

An optimal estimation based aerosol retrieval algorithm using OMI near-UV observations

Ukkyo Jeong¹, Jhoon Kim^{1,*}, Changwoo Ahn², Omar Torres³, Xiong Liu⁴, Pawan K. Bhartia³,
Robert J.D. Spurr⁵, David Haffner³, Kelly Chance⁴, and Brent N. Holben³

¹Dept. of Atmospheric Sciences, Yonsei University, Seoul, Korea

²Science Systems and Applications, Inc., Lanham, Maryland, USA

³Goddard Space Flight Center, NASA, Greenbelt, Maryland, USA

⁴Harvard-Smithsonian Center for Astrophysics, Cambridge, Massachusetts, USA

⁵RT Solutions, Inc., 9 Channing Street, Cambridge, Massachusetts, USA

*Corresponding author: Jhoon Kim (jkim2@yonsei.ac.kr)

Tel. +82-2-2123-5682, Fax. +82-2-365-5163

Abstract

An optimal estimation (OE) based aerosol retrieval algorithm using the OMI (Ozone Monitoring Instrument) near-ultraviolet observation was developed in this study. The OE-based algorithm has the merit of providing useful estimates of errors simultaneously with the inversion products. Furthermore, instead of using the traditional look-up tables for inversion, it performs online radiative transfer calculations with the Vector Linearized Discrete Ordinate Radiative Transfer (VLIDORT) model to eliminate interpolation errors and improve stability. The measurements and inversion products of the Distributed Regional Aerosol Gridded Observation Network campaign in Northeast Asia (DRAGON NE-Asia 2012) were used to validate the retrieved AOT and SSA. The retrieved AOT and SSA at 388 nm have a correlation with the Aerosol Robotic Network (AERONET) products that is comparable to or better than the correlation with the operational product during the campaign. The OE-based estimated error better represented the variance of actual biases of AOT at 388 nm between the retrieval and AERONET measurements than the operational error estimates. The forward model parameter errors were analyzed separately for both AOT and SSA retrievals. The surface reflectance at 388 nm, the imaginary part of the refractive index at 354 nm, and the number fine mode fraction (FMF) were found to be the most important parameters affecting the retrieval accuracy of AOT, while FMF was the most important parameter for the SSA retrieval. The additional information provided with the retrievals, including the estimated error and degrees of freedom, is expected to be valuable for relevant studies. Detailed advantages of using the OE method were described and discussed in this paper.

Key words

Aerosol; Error Analysis; Ozone Monitoring Instrument; Optimal Estimation Method; DRAGON campaign

1 **1. Introduction**

2 Anthropogenic aerosols have affected both the radiative and meteorological balance in the
3 atmosphere and thus the radiative forcing of the atmosphere directly and indirectly (Ramanathan et
4 al., 2001; Russell et al., 1999; Breon et al., 2002). To understand the role of aerosol in the
5 atmosphere from a global perspective, reliable aerosol data from satellites are essential (Al-Saadi et
6 al., 2005; Kinne et al., 2006). The several satellite-based [aerosol retrieval](#) methods based on multi-
7 wavelength (Levy et al., 2007; Kim et al., 2007), multi-angle (Fisher et al., 2014), active light
8 (Young et al., 2013), and polarization (Deuze et al., 2001) measurements have their own advantages
9 and limitations. [The inversion products from such measurements provide various parameters of
10 aerosols at different channels. Thus, appropriate sources of aerosol information need to be
11 employed for relevant studies.](#)

12 An important advantage of using the ultraviolet (UV) channel to retrieve aerosol optical
13 properties is that the results are less affected by uncertainties in surface reflectance (Torres et al.,
14 1998). The retrieved aerosol products have relatively uniform quality over both land and ocean
15 except over ice–snow surfaces (Torres et al., 2007; Herman et al., 1997). The near-UV technique for
16 aerosol remote sensing has the additional merit of a long term data record including aerosol
17 absorption properties of over 30 years starting from the launch of the Total Ozone Mapping
18 Spectrometer (TOMS) on Nimbus-7 in 1978 (Torres et al., 1998; Torres et al., 2002a; Torres et al.,
19 2005). Thus, the retrieved products using the near-UV technique from TOMS and Ozone
20 Monitoring Instrument (OMI) measurements are appropriate for climatological research (Torres et
21 al., 2002b; Torres et al., 2007). Information on aerosol extinction and absorption properties in the
22 UV region is also important for estimating the air mass factor (AMF) for trace gas retrievals
23 (Palmer et al., 2001; Lin et al., 2014). [However, deriving information on aerosol using available
24 hyperspectral measurements such as OMI and Global Ozone Monitoring Experiment \(GOME\) is
25 quite challenging due to the relatively low spatial resolution compared to typical imagers. Thus, the](#)

26 error estimates of retrievals using such sensors are particularly important to understand the
27 reliability of the information, so that it can be used appropriately. The main objective of this study
28 is to improve the applicability of the aerosol inversion products of OMI by providing the reliable
29 error estimates of the retrievals.

30 Accuracy assessments of the retrieved aerosol optical properties using UV radiances have
31 been performed by comparison with results from reference methods including ground, airborne, and
32 satellite based remote sensing techniques (Torres et al., 2005;Jethva et al., 2014;Torres et al.,
33 2002a;Ahn et al., 2014;Livingston et al., 2009;Ahn et al., 2008;Curier et al., 2008). The aerosol
34 information content of selected OMI spectral radiances using a multi-wavelength algorithm has
35 been estimated using principal component analysis for simulated radiances (Veihelmann et al.,
36 2007). Uncertainty estimates of UV aerosol retrievals have also been calculated by perturbation
37 analysis (Torres et al., 1998;Torres et al., 2002b). Inversion algorithms based on optimal estimation
38 (OE) theory provide not only a constrained solution with respect to the *a priori* information but also
39 detailed error analysis from well-categorized error sources (Rodgers, 2000). In addition, iterative
40 inversion methods such as OE provide additional retrieval masking parameters (e.g., cost function
41 and convergence criteria). Recently developed OE-based retrieval methods have provided both
42 improved inversion products and error estimates from the aerosol and surface error sources
43 (Wagner et al., 2010;Govaerts et al., 2010;Wurl et al., 2010).

44 A large amount of aerosol is emitted from both natural and anthropogenic sources in East
45 Asia (Lee et al., 2012). The spatial and temporal variations in aerosol optical properties are
46 significant because of the diverse emission sources and trans-boundary transport (Jeong et al., 2011).
47 Thus, the assumed aerosol inversion parameters may cause substantial uncertainties in the retrieval.
48 However, there are insufficient ground-based measurements of aerosol optical properties with
49 suitable spatial and temporal coverage in East Asia, despite their importance for global air quality
50 and climate change. The Distributed Regional Aerosol Gridded Observation Network Northeast

51 Asia (DRAGON-NE Asia) 2012 campaign ([http://aeronet.gsfc.nasa.gov/new_web/DRAGON-](http://aeronet.gsfc.nasa.gov/new_web/DRAGON-Asia_2012_Japan_South_Korea.html)
52 [Asia_2012_Japan_South_Korea.html](http://aeronet.gsfc.nasa.gov/new_web/DRAGON-Asia_2012_Japan_South_Korea.html)) provides valuable datasets including both urban and
53 regional-scale observations at more than 40 sites in Northeast Asia. In the present study, an OE-
54 based near-UV aerosol retrieval and error analysis algorithm is developed to provide both improved
55 aerosol inversion products and estimates of their uncertainties. The retrieved aerosol products and
56 estimated uncertainties are validated against the DRAGON-NE Asia 2012 campaign measurements.

57

58 **2. Data**

59 OMI is a nadir-viewing hyperspectral spectrometer aboard the EOS (Earth Observing
60 System)-Aura spacecraft that measures upwelling radiances from the top of the atmosphere in the
61 ultraviolet and visible (270–500 nm) regions with approximate spectral resolution of 0.5 nm (Levelt
62 et al., 2006). The advantage of using OMI for aerosol retrieval is its higher spatial resolution than
63 other UV hyperspectral spectrometers (from $13 \times 24 \text{ km}^2$ at nadir to $28 \times 150 \text{ km}^2$ at the swath
64 extremes with median pixel size $15 \times 32 \text{ km}^2$) together with its 2600-km-wide swath. The
65 radiometric calibration procedure and the estimated accuracy of OMI are described in Dobber et al.
66 (2006). To determine aerosol type and vertical distribution, the current OMI near-UV aerosol
67 algorithm (OMAERUV) employs the Cloud–Aerosol Lidar with Orthogonal Polarization (CALIOP)
68 monthly climatology of aerosol layer height and real-time Atmospheric Infrared Sounder (AIRS)
69 carbon monoxide (CO) observations (Torres et al., 2013). Surface reflectances at 354 nm and 388
70 nm were assumed to be Lambertian and were taken from the TOMS climatology database. Aerosol
71 vertical distribution and surface reflectance information identical to that used in the operational
72 algorithm were used for the OE-based algorithm here.

73 In this study, the spatial and temporal domains for analysis were confined to the
74 DRAGON-NE Asia 2012 campaign as shown in Figure 1 and Table 1. The gridded observation
75 networks had high spatial resolution over the representative megacities in Northeast Asia: Seoul in

76 South Korea and Osaka in Japan. To validate and compare the retrieved aerosol products from OMI,
77 level 2 campaign products were used from the aerosol robotic network (AERONET); 380 nm
78 aerosol optical thickness (AOT) from direct sun measurements and spectral single scattering albedo
79 (SSA) from almucantar inversion products (Holben et al., 1998;Dubovik and King, 2000;Dubovik
80 et al., 2000;Dubovik et al., 2006). Retrieved 388 nm AOT from OMI was validated against
81 AERONET 380 nm AOT. The OMI AOT retrievals within a radius of 0.5° of the AERONET site
82 and within ± 30 minutes of the OMI overpass time (about 13:40 local time) were averaged. The
83 resulting OMI AOT average values were then compared with the time-averaged Sun photometer
84 measurements.

85 Aerosol absorption properties are retrieved at different wavelengths by AERONET and
86 OMI. The AERONET inversion products of the SSA are available at 440, 670, 860, and 1020 nm,
87 while the OMAERUV algorithm retrieves the SSA at 354 nm and 388 nm. Earlier field studies
88 found that aerosol absorption is a continuous function of wavelength in the ultraviolet to short
89 infrared region (Kirchstetter et al., 2004;Russell et al., 2010). To compare the SSA values from
90 OMI and AERONET at the same wavelength, the AERONET SSA at 388 nm was obtained by
91 extrapolating the SSAs at 440–1020 nm using a spline function. Then the converted AERONET
92 SSA at 388 nm was compared with the retrieved OMI SSA values even though uncertainties might
93 exist in the transformation. Unlike the direct sun measurements including AOT, the inversion
94 products of AERONET from almucantar measurements are retrieved less frequently and require
95 appropriate atmospheric conditions for AOT (440 nm AOT > 0.4) and solar zenith angle (solar
96 zenith angle > 45°) (Dubovik and King, 2000;Jethva et al., 2014). Such favorable atmospheric
97 conditions for the inversion using almucantar measurements rarely overlap closely with the OMI
98 overpass time. Furthermore, too narrow a time window around the satellite overpass time reduces
99 the number of comparison samples. In this study, to secure enough data points the SSA of a region
100 at OMI overpass time was assumed to adequately represent the daily values. For the comparison,

101 the converted 388 nm SSA from AERONET was averaged over a day and the OMI retrievals of 388
102 nm SSA were spatially averaged over a grid area of $0.5^\circ \times 0.5^\circ$ centered on the AERONET site.

103

104 **3. Method**

105 **3.1. Operational OMI near UV aerosol algorithm**

106 The OMAERUV uses two channel radiances at 354 nm and 388 nm to estimate aerosol
107 amount and absorption properties (Torres et al., 1998; Torres et al., 2007; Torres et al., 2013). AOT
108 and SSA at 388 nm are retrieved from pre-calculated reflectance look-up tables (LUT) for pre-
109 determined nodal points of observational geometry and aerosol optical properties, total optical
110 depth, and aerosol layer height. Three major aerosol types are considered and listed in Table 2:
111 desert dust, carbonaceous aerosols associated with biomass burning, and weakly absorbing sulfate-
112 based aerosols (hereafter dust, smoke, and sulfate, respectively). Each aerosol type has an assumed
113 particle size distribution (PSD) derived from the long-term statistics of AERONET inversion
114 products. The UV real refractive index (n_r) is obtained from the Optical Properties Of Aerosols And
115 Clouds (OPAC) database (Hess et al., 1998). In the operational algorithm, the imaginary refractive
116 indices (n_i) at 354 nm are assumed to be 1.0, 1.2, and 1.4 times the retrieved n_i at 388 nm for sulfate,
117 smoke, and dust aerosol, respectively (Torres et al., 2007; Jethva and Torres, 2011). [The overall
118 concept and design of the improved OMAERUV algorithm is well described by Torres et al. \(2013\).](#)

119 There have been further improvements at updated OMAERUV (version 1.5.3), which was
120 used for reprocessing the data of AOT and SSA in this study. The OMAERUV algorithm was
121 refined by adjusting thresholds of UV aerosol index (UVAI) and Atmospheric Infrared Sounder
122 (AIRS) CO data in determining aerosol types and retrieval approaches. A cloud screening scheme
123 in assigning algorithm quality flags was also modified for retaining more good retrievals of
124 carbonaceous and sulfate type aerosols when the CO level is high enough (higher than 3.2×10^{18}
125 molecules $\cdot\text{cm}^{-2}$) with various reflectivity thresholds. The UVAI threshold was changed from 0.8 to

126 0.5 over the oceans. This modification eliminates the land-ocean discontinuity in UVAI threshold. It
127 is now identical (0.5) for both conditions. The current characterization of ocean reflective properties
128 in the OMAERUV algorithm does not explicitly account for ocean color effects and, therefore, the
129 quality of the retrieved aerosol properties over the oceans for low aerosol amounts would be highly
130 uncertain. For that reason, retrievals over the oceans are only carried out for high concentrations of
131 either desert dust or carbonaceous aerosols as indicated by UVAI values larger than or equal to 0.5.

132 Depending on the magnitude of the UVAI and CO parameters as well as the aerosol type,
133 two retrieval approaches are currently used. They are referred to as two-channel and single-channel
134 retrievals. In the two-channel approach, observations at 354 and 388 nm are used to simultaneously
135 derive AOD and SSA. Over scenes when the aerosol absorption signal is low, the single-channel
136 retrieval is applied. AOD is retrieved from the 388 nm observation assuming a value of 1.0 for SSA.
137 Different CO threshold values are used for the northern and southern hemispheres to remove upper
138 tropospheric CO which may not be necessarily associated with carbonaceous aerosols. A smoothing
139 function in CO is used to transition from SH to NH threshold values. Specific criteria for retrieval
140 approaches are summarized in Table 3. More detailed information of the latest update in
141 OMAERUV is available from the Readme file at the web site
142 (http://disc.sci.gsfc.nasa.gov/Aura/data-holdings/OMI/omaeruv_v003.shtml).

143

144 **3.2. OE-based OMI near UV aerosol algorithm**

145 The traditional LUT-based inversion method potentially includes errors due to interpolation
146 between the nodal points and the local minimum, despite its high numerical efficiency. Such
147 interpolation error typically depends on the interpolation method, number of the nodal points, and
148 analytic characteristics of the parameters in LUT. In order to reduce the interpolation error, higher
149 resolution of LUT nodal points is necessary which requires larger amount of numerical computation.
150 Furthermore, in order to modify the retrieval algorithm, whole LUT should be re-calculated even

151 for a few number of target retrievals. The errors from the interpolation are also hard to evaluate as
152 the LUT becomes more complicated.

153 On the contrary, online retrieval methods can reduce such errors from the interpolation and
154 are numerically efficient particularly for the smaller number of target retrievals. Thus, online
155 retrieval method is appropriate for the research purposes since retrieval sensitivity study typically
156 use smaller number of sample compared to the operational purposes and prefer rapid and accurate
157 results. In our experience, the online retrieval method was numerically more efficient compared to
158 the LUT-based retrieval method by order of 1 or 2 for less than few thousands of retrievals.
159 Furthermore, the online retrieval methods are optimized to avoid local minima by employing
160 additional constraints to find more reliable and stable solutions (Kalman, 1960;Phillips,
161 1962;Tikhonov, 1963;Twomey, 1963;Chahine, 1968). However, employing online calculation as
162 operational retrieval method requires large computation cost. Thus, using the online calculation as a
163 benchmark results for the LUT-based algorithm is recommended to develop the optimized LUT for
164 the operational purposes. Recent efforts to minimize the numerical cost of radiative transfer model
165 and to increased calculation speed are expected to make the online calculation more practical even
166 for the operational purposes.

167 Optimization for measurement error, the inclusion of *a priori* and ancillary data, and
168 employing physical constraints (*e.g.*, non-negativity of measurements and retrievals) for an
169 inversion method are important since each method has its own advantages and disadvantages
170 (Dubovik, 2004). In this study, we used OE as the inversion method (Rodgers, 2000) since it has
171 several advantages over other methods for OMI-like measurements, as discussed in Section 4. The
172 atmospheric inverse problem often suffers from both insufficient information content of the
173 measurements and imperfect measurement accuracy. Bayesian statistics provides mapping methods
174 from the measurement probability density function (pdf) into state space with prior knowledge.
175 Based on Bayes' theorem, the OE technique employs additional constraints from external sources (*a*

176 *priori*) to complement the insufficient information content of the measurements. For the nonlinear
 177 inversion case, by considering the maximum *a posteriori* approach, the general form of the
 178 Bayesian solution can be expressed as Equation (1) where measurement and *a priori* errors are
 179 assumed to be Gaussian (Rodgers, 2000):

$$181 \quad -2\ln P(\mathbf{x}|\mathbf{y}) = [\mathbf{y} - \mathbf{K}\mathbf{x}]^T \mathbf{S}_\epsilon^{-1} [\mathbf{y} - \mathbf{K}\mathbf{x}] + [\mathbf{x} - \mathbf{x}_a]^T \mathbf{S}_a^{-1} [\mathbf{x} - \mathbf{x}_a] + \mathbf{c} \quad (1)$$

182
 183 where \mathbf{x} is the state vector and \mathbf{y} the measurement vector, \mathbf{K} is the weighting function matrix,
 184 \mathbf{S}_ϵ is the measurement error covariance matrix, \mathbf{x}_a is the *a priori* mean state, and \mathbf{S}_a is the *a*
 185 *priori* covariance matrix. The formulation finds the optimized solution that minimizes the cost
 186 function (χ):

$$187 \quad \chi^2 = \left\| \mathbf{S}_\epsilon^{-\frac{1}{2}} (\mathbf{y} - \mathbf{K}\mathbf{x}) \right\|_2^2 + \left\| \mathbf{S}_a^{-\frac{1}{2}} (\mathbf{x} - \mathbf{x}_a) \right\|_2^2 \quad (2)$$

188
 189 Detailed derivations and implications are described in previous studies (Rodgers, 2000; Wurl et al.,
 190 2010; Govaerts et al., 2010). As described above, the OMI near-UV algorithm uses radiance (I_{388})
 191 and spectral contrast (I_{354}/I_{388}) for the measurement vector, where I_{354} and I_{388} are the
 192 normalized radiances at 354 nm and 388 nm, respectively. The state vector in this study is the AOT
 193 at 388 nm (τ_{388}) and the imaginary refractive index at 388 nm ($n_{i,388}$). Then, the weighting
 194 function matrix can be expressed as follows:

$$195 \quad \mathbf{K} = \begin{bmatrix} \frac{\partial I_{388}}{\partial \tau_{388}} & \frac{\partial I_{388}}{\partial n_{i,388}} \\ \frac{\partial}{\partial \tau_{388}} \left(\frac{I_{354}}{I_{388}} \right) & \frac{\partial}{\partial n_{i,388}} \left(\frac{I_{354}}{I_{388}} \right) \end{bmatrix} \quad (3)$$

196

197 where the weighting function of the spectral contrast can be obtained from the following derivative:

198

$$\frac{\partial}{\partial x} \left(\frac{I_{354}}{I_{388}} \right) = \frac{\frac{\partial I_{354}}{\partial x} I_{388} - I_{354} \frac{\partial I_{388}}{\partial x}}{(I_{388})^2} \quad (4)$$

199

200 In typical inversion methods, including OE, estimation of the reliable measurement error
201 covariance matrix is important to determine the likelihood of the solution (Govaerts et al., 2010).
202 The measurement error includes radiometric noise error and calibration accuracy. The absolute
203 bidirectional scattering distribution function (BSDF) radiometric accuracy of the OMI instrument is
204 reported to be about 4% for 2σ and the random noise error is provided in the level 1b product
205 (Dobber et al., 2006). However, the reported BSDF uncertainty includes the errors in the calibration
206 method and it represents whole wavelength domain. Thus, actual BSDF uncertainty at 354 and 388
207 nm would be less than 2% (Jaross, 2015). In our experience, 2% of BSDF uncertainty leads to the
208 overestimates of the error and it is still challenging to evaluate. According to multiple retrieval tests,
209 the BSDF uncertainty was assumed to be 1% in this study. The radiometric error covariance at each
210 wavelength was calculated from the square root of the sum of squared radiometric uncertainty and
211 calibration accuracy. The error covariance matrix can be written as:

212

$$\mathbf{S}_\epsilon = \begin{bmatrix} \sigma(\epsilon_{388})^2 & \sigma(\epsilon_{388}, \epsilon_{354/388})^2 \\ \sigma(\epsilon_{388}, \epsilon_{354/388})^2 & \sigma(\epsilon_{354/388})^2 \end{bmatrix} \quad (5)$$

213

214 where ϵ_λ is the total error of the measured radiance at wavelength λ , $\epsilon_{354/388}$ is the error of
 215 I_{354}/I_{388} , which is described later in this section, and $\sigma(\epsilon_{388}, \epsilon_{354/388})^2$ is the covariance
 216 between the total measurement errors of I_{388} and I_{354}/I_{388} .

217 The ϵ_λ typically includes both random and systematic components and its covariance can
 218 be expressed as follows:

219

$$\sigma(\epsilon_\lambda)^2 = \sigma(\epsilon_{r,\lambda})^2 + \sigma(\epsilon_{s,\lambda})^2 \quad (6)$$

220

221 where $\epsilon_{r,\lambda}$ and $\epsilon_{s,\lambda}$ are the random and systematic components of radiometric error at λ , and
 222 $\sigma(\epsilon_{r,\lambda})^2$ and $\sigma(\epsilon_{s,\lambda})^2$ are their covariance values, respectively. The $\epsilon_{354/388}$ can be
 223 approximated as follows:

224

$$\epsilon_{354/388} \cong \frac{I_{354}}{I_{388}} - \frac{I_{354} + \epsilon_{354}}{I_{388} + \epsilon_{388}} \cong \frac{I_{354}}{I_{388}} \left(\frac{\epsilon_{354}}{I_{354}} - \frac{\epsilon_{388}}{I_{388}} \right) \cong \frac{I_{354}}{I_{388}} \left(\frac{\epsilon_{s,354}}{I_{354}} - \frac{\epsilon_{s,388}}{I_{388}} + \frac{\epsilon_{r,354}}{I_{354}} - \frac{\epsilon_{r,388}}{I_{388}} \right) \quad (7)$$

225

226 When the systematic components of the measurement errors of radiances at 354 nm and 388 nm are
 227 positively correlated and their values are similar, part of the systematic uncertainties can be reduced

228 by the $\frac{\epsilon_{s,354}}{I_{354}} - \frac{\epsilon_{s,388}}{I_{388}}$ term. However, assessment of the systematic error of OMI measurements at

229 each pixel is still challenging despite this partial reduction of systematic errors by using I_{354}/I_{388} .

230 In this study, the BSDF calibration uncertainties of I_{354} and I_{388} at a pixel are assumed to be

231 systematic and similar, while the radiometric noise values of I_{354} and I_{388} are assumed to be

232 random and independent. Then, the systematic measurement error of $\epsilon_{354/388}$ can be regarded as

233 negligible and the covariance of $\epsilon_{354/388}$ in Equation (7) can be approximated as follows:

234

$$\sigma(\epsilon_{354/388}) \cong \frac{I_{354}}{I_{388}} \sqrt{\left(\frac{\epsilon_{r,354}}{I_{354}}\right)^2 + \left(\frac{\epsilon_{r,388}}{I_{388}}\right)^2} \quad (8)$$

235

236 The $\sigma(\epsilon_{388}, \epsilon_{354/388})^2$ can be obtained as follows:

237

$$\sigma(\epsilon_{388}, \epsilon_{354/388})^2 = \frac{1}{n-1} \sum_{i=1}^n \epsilon_{388}^i \epsilon_{354/388}^i \quad (9)$$

238

239 where ϵ_{388}^i and $\epsilon_{354/388}^i$ are the uncertainties in the i^{th} measurement of I_{388} and I_{354}/I_{388} for
 240 a sample of size n , respectively. Under the same assumptions used in Equations (7) and (8),
 241 $\epsilon_{354/388}^i$ has only random and independent components, and so $\sigma(\epsilon_{388}, \epsilon_{354/388})$ can be regarded
 242 as negligible. The diagonal and off-diagonal elements of the measurement error covariance matrices
 243 using two different measurement matrices are compared in Table 4.

244

245 3.3. Error characterization

246 Retrieved products with estimated and/or characterized error are valuable for any
 247 application. Various error sources can be categorized as shown in the following equation by
 248 linearizing the forward model with respect to associated parameters (Eyre, 1987; Rodgers, 1990,
 249 2000):

250

$$\hat{\mathbf{x}} - \mathbf{x} = (\mathbf{A} - \mathbf{I}_n)(\mathbf{x} - \mathbf{x}_a) + \mathbf{G}_y \mathbf{K}_b (\mathbf{b} - \hat{\mathbf{b}}) + \mathbf{G}_y \Delta \mathbf{f}(\mathbf{x}, \mathbf{b}, \mathbf{b}') + \mathbf{G}_y \boldsymbol{\epsilon} \quad (10)$$

251

252 where $\hat{\mathbf{x}}$ and \mathbf{x} are the retrieval and true states, respectively; \mathbf{A} is the averaging kernel matrix; \mathbf{I}_n
 253 is the identity matrix; \mathbf{x}_a is the *a priori* state vector; \mathbf{G}_y is the contribution function matrix; \mathbf{K}_b

254 is the weighting function matrix of forward model parameters (\mathbf{b}); $\hat{\mathbf{b}}$ is the guessed forward model
 255 parameter; $\Delta\mathbf{f}$ is the error in the forward model relative to the real physics; and ϵ is the
 256 measurement error. The first and last term on the right-hand-side (RHS) of Equation (10) is the
 257 smoothing error and retrieval noise, respectively. Their covariance matrices can be calculated from:
 258

$$\mathbf{S}_s = (\mathbf{A} - \mathbf{I}_n)\mathbf{S}_E(\mathbf{A} - \mathbf{I}_n)^T \quad (11)$$

$$\mathbf{S}_n = \mathbf{G}_y\mathbf{S}_\epsilon\mathbf{G}_y^T \quad (12)$$

259
 260 where \mathbf{S}_s is the smoothing error covariance matrix, \mathbf{S}_E is the covariance of the ensemble of states
 261 about the mean state, and \mathbf{S}_n is the covariance matrix of the retrieval noise. We have assumed that
 262 the climatological value is a good representation of the real ensemble of the state about the mean
 263 state, and so the covariance matrix of the *a priori* state was employed as the \mathbf{S}_E in this study. Each
 264 \mathbf{S}_s and \mathbf{S}_n has two diagonal elements that represent the variances of the smoothing error and
 265 retrieval noise for two retrievals, AOT and SSA. The smoothing error (ϵ_{sm}) and retrieval noise (ϵ_n)
 266 of AOT and SSA were defined as the square root of the corresponding diagonal elements of \mathbf{S}_s and
 267 \mathbf{S}_n , respectively. The square root of the sum of squared ϵ_{sm} and ϵ_n of AOT and SSA are defined
 268 in this study as the solution errors (ϵ_{sol}) of AOT and SSA, respectively.

269 The second term on the RHS of Equation (10) is the forward model parameter error, and its
 270 covariance matrix can be calculated as follows:

271

$$\mathbf{S}_f = \mathbf{G}_y\mathbf{K}_b\mathbf{S}_b\mathbf{K}_b^T\mathbf{G}_y^T \quad (13)$$

272

273 where \mathbf{S}_f is the covariance matrix of the forward model parameter error, and \mathbf{S}_b is the error
 274 covariance matrix of forward model parameter, \mathbf{b} . The forward model parameters of the near-UV
 275 method include the aerosol microphysical model parameters, aerosol vertical distribution,

276 meteorological profile (pressure and temperature), and surface properties. These forward model
277 parameters contain both random and systematic components with different scales of spatial and
278 temporal variation. Furthermore, each forward model parameter has a different uncertainty that is
279 difficult to evaluate. In this study, \mathbf{S}_f was analyzed separately with respect to each forward model
280 parameter as suggested by Rodgers (2000). The forward model parameter error (ϵ_f) of AOT and
281 SSA were obtained from the square root of the corresponding diagonal elements of each \mathbf{S}_f .

282 The third term on the RHS in Equation (10) is the forward model error that is caused by
283 discrepancies between known and real physics. To simulate the earth-reflected radiance, VLIDORT
284 (linearized pseudo-spherical vector discrete ordinate radiative transfer code, version 2.6) was used.
285 This code is based on one of the most accurate radiative transfer solutions for a one-dimensional
286 atmosphere (Spurr, 2006). Linearization of state vectors and forward model parameters are
287 described in prior papers (Spurr et al., 2012; Spurr and Christi, 2014). Although the simulated
288 radiances are expected to be accurate, the forward model error depends on factors including the
289 number of streams, layers, and Legendre coefficients for the aerosol phase functions. To reduce the
290 numerical errors that can arise from an insufficient number of coefficients, 3 Stokes parameters, 75
291 layers, 16 streams, and up to 500 Legendre coefficients for the aerosol phase matrix were used for
292 the radiance simulations. However, it is still a challenge to evaluate other possible sources of
293 forward model error such as Raman scattering and the three-dimensional effect of the atmosphere
294 for retrieval. Such issues are beyond the scope of this study, and thus only smoothing error, retrieval
295 noise, and forward model parameter error are evaluated here.

296

297 **3.4. *A priori* characterization**

298 Using reliable *a priori* information is important in the OE method since the final solutions
299 are determined between the *a priori* state and the inversion space of a measurement. There are
300 several sources of *a priori* information including climatological data, reliable measurements from

301 more accurate instruments, and calculations from models based on theoretical or empirical statistics
302 (Govaerts et al., 2010;Wurl et al., 2010;Rodgers, 2000). Appropriate sources of *a priori* depend on
303 the characteristics of the state vector and the accuracy of the *a priori* database. When the *a priori*
304 state has a systematic bias away from the true state, this bias propagates to the retrieval products. In
305 this study, 10 years (from 2005 to 2014) of OMAERUV 388 nm AOT and SSA in spring (from
306 March to May) were used for the *a priori* data. Figure 2 shows the collected climatological data of
307 the 388 nm AOT and SSA in East Asia used in this study. To avoid biases due to cloud
308 contamination in the OMI products, averaged values and standard deviations (σ) with more than 70
309 data points were used.

310

311 **4. Results**

312 The dust event on 28th April 2012 has been selected to compare the aerosol optical
313 properties from the operational product with the OE-based retrievals in this study. Figure 3 shows
314 the true color image on that day from the Moderate Resolution Imaging Spectroradiometer (MODIS)
315 Aqua and the UV aerosol index from OMI. To see the difference between the OE-based and
316 operational algorithm in the same area, both methods were applied to measurements with an
317 operational algorithm flag of 0, to avoid cloud contamination and radiometric calibration
318 uncertainties. Some of the points retrieved by the operational algorithm were rejected in the OE-
319 based retrievals when the cost function cut-off was applied, as described in this section.

320 The AOT and SSA at 388 nm from the operational and OE-based products are compared in
321 Figure 4. The ε_{sol} of the retrieved AOT and SSA at 388 nm, degree of freedom, and χ are shown
322 in Figure 5. The OE-based and operational AOT at 388 nm are similar, as shown in Figure 4 (a) and
323 (b). Both products seem to be affected by snow and cloud contaminated pixels around Seoul in
324 South Korea (37°N, 126°E), Tianjin in China (39°N, 116°E) and Nagano in Japan (36°N, 138°E).
325 In Figure 5 (a), the ε_{sol} of retrieved AOT at 388 nm has relatively high values compared with the

326 AOT level at large viewing zenith angle. Noticeable discrepancies of SSA at 388 nm from the
327 operational and OE-based products are evident in some of the areas as shown in Figure 4 (c) and (d).
328 The operational algorithm performed single-channel retrieval around East Mongolia (47°N, 115°E),
329 while the OE-based algorithm performed two-channel retrieval for all cases. Since this area has a
330 low level of AOT, the information content of aerosol absorption property is insufficient, resulting in
331 the low degrees of freedom shown in Figure 4 (b) and Figure 5 (c). Thus the OE-based SSA in this
332 area (Figure 4 (d)) seems noisy and the ε_{sol} of SSA appears high. Similar results for the behavior
333 of SSA are apparent around central Japan (38°N, 138°E). Thus, SSA values with high AOT and low
334 ε_{sol} are recommended for the analysis, similar to the retrieval conditions for AERONET inversion
335 products (Dubovik and King, 2000). Additional information provided on retrievals at each pixel in
336 Figure 5 is expected to be valuable for relevant studies including trace gas retrieval and data
337 assimilation.

338 Figure 6 shows the results of validation of operational and OE-based AOT retrievals at 388
339 nm. As shown in Figure 6 (a) and (b), the OE-based inversion method showed higher correlation
340 coefficient ($r = 0.82$) and slightly improved slope (0.83) and offset (0.16) values than the
341 operational algorithm ($r = 0.71$, slope = 0.71, and offset = 0.2). The Fisher's z -value between the
342 correlation coefficients (Fisher, 1921) was 3.04 corresponding to two-tailed p -value of 0.0024. The
343 Student's t -value for the difference between the two slopes is 2.10 with 512 degrees of freedom
344 with the two-tailed p -value of 0.04. The statistical values show that difference between the two
345 correlation coefficients and slopes are significant (p -value < 0.05). The Q values (percentage of
346 AOT retrievals falling within an uncertainty envelope of $\pm 30\%$ or 0.1) of the OE-based retrievals
347 and operational algorithm were similar (63.0%). When a measured radiance is affected by
348 parameters that the theoretical radiative transfer model does not consider (*e.g.*, sub-pixel cloud
349 contamination), the χ of the retrieval typically has a high value. In this study, retrievals with χ larger
350 than a certain value (*i.e.*, 2.0 in this study) have been rejected. This limitation on retrievals imposed

351 by the χ reduced the number of retrievals with abnormally high biases, which might be associated
352 with sub-pixel cloud contamination, in the operational algorithm in Figure 6 (a).

353 The SSA values at 388 nm from OMI operational products and OE-based inversion
354 products were compared with those at 388 nm and 440 nm from AERONET inversion products as
355 shown in Figure 7. The retrieved SSA at 388 nm from the operational algorithm showed
356 comparable or higher values of $Q_{0.03}$ (59.2%) and $Q_{0.05}$ (85.1%) with those from the OE-based
357 algorithm ($Q_{0.03} = 53.5\%$, $Q_{0.05} = 86.0\%$) when compared with the AERONET SSA at 440 nm (The
358 $Q_{0.03}$ and $Q_{0.05}$ represent the percentage of SSA retrievals falling within an uncertainty envelope of
359 ± 0.03 and ± 0.05 , respectively). The retrieved 388 nm SSA from both the operational and OE-based
360 algorithms showed similar correlation with the AERONET ($r = 0.27$ and 0.26 for operational and
361 OE-based algorithms, respectively. Fisher's z -value is 0.1 with two-tailed p -value of 0.92). The
362 retrieved SSA at 388 nm from the operational and OE-based algorithms showed slightly higher
363 correlation with the converted 388 nm SSA from AERONET ($r = 0.34$ and 0.33 for the operational
364 and OE-based algorithm, respectively) than with the 440 nm SSA from AERONET. However, the
365 significances of the differences in r between converted and unconverted SSA comparisons were low
366 (Fisher's z -values were 0.71 and 0.67 with two-tailed p -values of 0.48 and 0.50 for operational
367 algorithm and OE-based algorithm, respectively). The retrieved SSA at 388 nm from the
368 operational algorithm also showed comparable or higher values of $Q_{0.03}$ (59.2%) and $Q_{0.05}$ (83.9%)
369 than those of the OE-based algorithm ($Q_{0.03} = 53.5\%$, $Q_{0.05} = 82.8\%$) when compared with
370 converted SSA at 388 nm from AERONET.

371 The estimated retrieval uncertainties of the AOT at 388 nm from the operational algorithm
372 (ϵ_{omi} , $\pm 30\%$ or 0.1) and estimated ϵ_{sol} were plotted against the biases relative to AERONET
373 measurements as shown in Figure 8. The percentages of AOT retrieval biases from AERONET
374 falling within the estimated retrieval errors of operational (Q_{omi}) and OE-based method (Q_{sol}) were
375 64.8% and 65.9%, respectively. The Q_{sol} was higher than Q_{omi} despite of the lower mean value of

376 ε_{sol} (0.20) than that of ε_{omi} (0.21). The error bars and black squares in Figure 8 represent the
377 moving σ and average value of the retrieval biases from AERONET as a function of estimated error,
378 respectively. As shown in Figure 8 (b), ε_{sol} better explained the moving σ of the actual biases
379 ($r=0.93$) than ε_{omi} in Figure 8 (a) ($r=0.52$). Fisher's z -value between the correlation coefficients
380 was 2.33 with two-tailed p -value of 0.02. The systematic biases of ε_{sol} and ε_{omi} (represented by
381 the moving average of each error estimates) are typically related to other error sources, including
382 forward model parameters and sub-pixel cloud contaminations. Since the ε_{sol} of retrieved AOT
383 considers the theoretical sensitivity of the retrieval biases to associated parameters, it explained the
384 retrieval uncertainties better than the ε_{omi} , which only considers the retrieved AOT values.

385 Table 5 shows the suggested error sources and their magnitudes from the OMI ATBD
386 (Algorithm Theoretical Basis Documents) (Torres et al., 2002b) and the values employed in this
387 study. Although the current OMI cloud masking method is based on long-term TOMS heritage,
388 there may still be ground pixels contaminated by sub-pixel clouds. As the TOA reflectance is
389 greatly increased by even a small amount of cloud, cloud contamination can cause large positive
390 biases in the AOT retrieval. Previous studies estimated the AOT retrieval errors due to 5% cloud
391 contamination to be of the order of 0.1 to 0.2 (Torres et al., 1998; Torres et al., 2002b). They also
392 reported an even higher error in the single scattering albedo (0 to 0.15) especially for strongly
393 absorbing aerosols. However, estimation of sub-pixel cloud contamination is difficult because of the
394 large spatio-temporal variability of clouds and the relatively large ground pixel size of OMI. Thus
395 the further error analysis of cloud contamination error budget from Torres et al. (2002b) was not
396 performed in this study. Typical uncertainties of the 354 nm and 388 nm surface reflectances were
397 assumed to be 0.01 for both land and ocean. The BSDF accuracy was assumed to be 1% (Dobber et
398 al., 2006; Jaross, 2015), and radiometric precision from OMI Level 1b data. To analyze the
399 uncertainty associated with the aerosol size information and refractive index, σ values of the size
400 parameter and n_r at 440 nm were taken from AERONET inversion products during the campaign

401 period. To analyze the assumed n_i at 354 nm, the S_b was also obtained from AERONET statistics
402 during the campaign period. Aerosol vertical distribution is important as it affects aerosol retrieval
403 using near-UV and blue channels, particularly for absorbing aerosols (Torres et al., 1998; de Graaf
404 et al., 2005; Torres et al., 2013). However, accuracy assessments of the aerosol height information
405 used are still challenging. Typical uncertainties of the assumed aerosol layer peak height and half
406 width were assumed to be 2 km and 1 km, respectively, in this study. In the OE-based near-UV
407 aerosol retrieval algorithm, all aerosols are assumed to be spherical and the optical properties are
408 calculated from aerosol microphysical properties using the Mie solution. However, non-sphericity
409 may cause significant uncertainties, especially for large particles (Mishchenko and Travis,
410 1994; Mishchenko et al., 1995; Mishchenko et al., 1997; Mishchenko et al., 2003; Dubovik et al.,
411 2006), and aerosol morphology is quite complicated and requires further analysis for the near-UV
412 region. This is out of the scope of this study and thus needs to be investigated in a future study.
413 Therefore the uncertainties due to aerosol non-sphericity were not analyzed.

414 Figure 9 shows the average and σ values of ε_f of the retrieved AOT and SSA that were
415 sampled for the validation in Figure 6 (b) and Figure 7 (b), (d). High values of ε_f for AOT
416 appeared in n_i at 354 nm (0.34 ± 0.25), surface reflectance at 388 nm (0.19 ± 0.07), and the number
417 fine mode fraction (FMF) (0.16 ± 0.09). These values are higher or comparable with the mean ε_{sol}
418 of retrieved AOT at 388 nm (0.20). Thus, the accuracy of AOT retrievals depends on not only the
419 radiometric accuracy and information content but also the aerosol models and ancillary data of the
420 surface reflectance, of which the effect is already well known. The FMFs of the sulfate (0.999596)
421 and smoke type aerosols (0.999795) are similar while that for dust type aerosols is quite different
422 (0.995650). Considering that the estimated σ value for FMF uncertainty in this study (0.0015, see
423 Table 5) is much lower than the difference between the FMFs of dust type and other aerosols
424 (~ 0.004 , see Table 2), the errors resulting from selection of the wrong aerosol type can be more
425 significant. The estimated ε_f of the surface reflectance at 388 nm was higher than the previously

426 suggested value (0.07–0.09 for AOT and <0.01 for SSA) in the OMI ATBD (Torres et al., 2002b).
427 The ε_f s of AOT with respect to the surface reflectance at 354 nm (0.12±0.04), peak height of the
428 aerosol vertical distribution (0.11±0.10), fine mode n_r (0.09±0.10), half width of the fine mode PSD
429 (0.07±0.06), mean radius of the coarse mode PSD (0.06±0.03), and half width of the aerosol
430 vertical distribution (0.06±0.05) showed similar moderate sensitivity. Those for the mean radius of
431 the fine mode PSD (0.02±0.02) and half width of the coarse mode PSD (0.02±0.01) were smaller
432 and that of the coarse mode n_r (0.003±0.004) was found to be negligible.

433 Among ε_f s of the SSA retrieval, the FMF error ($1.4 \times 10^{-2} \pm 6.4 \times 10^{-3}$) was the most
434 important of the ε_f s of the SSA retrieval. Errors in n_i at 354 nm ($7.4 \times 10^{-3} \pm 2.8 \times 10^{-3}$) and the peak
435 height of the aerosol vertical distribution ($5.2 \times 10^{-3} \pm 2.8 \times 10^{-3}$) were found to be the second most
436 important. The ε_f of SSA with respect to the fine mode n_r ($3.9 \times 10^{-3} \pm 1.7 \times 10^{-3}$), width of the fine
437 mode PSD ($3.8 \times 10^{-3} \pm 1.7 \times 10^{-3}$), the surface reflectance at 354 nm ($3.4 \times 10^{-3} \pm 1.8 \times 10^{-3}$) and 388
438 nm ($2.8 \times 10^{-3} \pm 2.1 \times 10^{-1}$), mean radius of the coarse mode PSD ($3.1 \times 10^{-3} \pm 1.1 \times 10^{-3}$), half width of
439 the aerosol vertical distribution ($2.3 \times 10^{-3} \pm 1.5 \times 10^{-3}$), mean radius of the fine mode PSD (1.1×10^{-3}
440 $\pm 5.7 \times 10^{-4}$) and width of the coarse mode PSD ($8.7 \times 10^{-4} \pm 3.3 \times 10^{-4}$) were smaller and that of the
441 coarse mode n_r ($5.2 \times 10^{-5} \pm 1.3 \times 10^{-4}$) appeared to be negligible. The estimated ε_f s of SSA were
442 found to be about a factor magnitude lower than the ε_{sol} of SSA. The mean values of ε_{sm} and ε_n
443 of SSA were 0.023 and 0.029, respectively. Thus, the estimated ε_{sol} of SSA at 388 nm is expected
444 to be more reliable and represent the total uncertainties of SSA, since the uncertainty in SSA is
445 predominantly affected by ε_{sol} , while uncertainty in AOT is affected by both ε_{sol} and ε_f . **Note**
446 **that the relative significances of the ε_f s of retrievals depend on their condition. It is additional**
447 **merit of the error analysis using OE method that it provides specific error estimates of individual**
448 **target event retrieval (e.g., dust or biomass burning event). While analysis studies using satellite**
449 **inversion products have often suffered from the statistic reliabilities, more reliable error estimates in**
450 **this study are expected to contribute to the assessment of significances of the analysis.**

451

452 **5. Summary and Discussion**

453 An OE-based aerosol retrieval and error characterization algorithm using the OMI near-UV
454 radiances was developed in this study. The climatological values of OMAERUV products were
455 employed as *a priori* data for the inversion method. The OE-based inversion method developed
456 here provides not only the retrieved values of AOT and SSA but also estimates of their uncertainties.
457 The retrieved AOT and SSA at 388 nm were compared with the AERONET products during the
458 DRAGON-NE Asia 2012 campaign. The retrieved AOT using the OE method showed better results
459 than the operational product. The OE-based SSA at 388 nm showed consistency with AERONET
460 inversion products comparable to that of the operational SSA. The estimated retrieval noise and
461 smoothing error of OE-based AOT represented well the **variances of** actual biases between the
462 retrieved AOT and AERONET AOT. The forward model parameter errors were analyzed separately
463 for both AOT and SSA inversion products. Uncertainties of surface **reflectance** at 388 nm,
464 imaginary refractive index at 354 nm and number fine mode fraction were found to be the most
465 important parameters affecting the retrieval accuracy of AOT, while uncertainties in the coarse
466 mode real part of the refractive index had negligible effect. For SSA retrieval accuracy, number fine
467 mode fraction was found to be the most important parameter while the other parameters appeared to
468 have relatively small effects. As the FMF depends on the aerosol type, it is expected that more
469 accurate aerosol type classification might improve the retrieval accuracy of AOT and SSA. For
470 AOT retrieval, the estimated ε_f was comparable with the ε_{sol} , while the ε_f of SSA was
471 negligible compared to the ε_{sol} of the retrieved SSA. It is also found that a sufficient amount of
472 aerosol loading is necessary for reliable SSA retrieval.

473 However, there are still error sources which need to be analyzed, including the *a priori* error
474 from climatology, aerosol morphology, cloud contamination, and three dimensional effects of
475 radiative transfer. The assumed conditions in the inversion procedure also differ from the real state.

476 Validation studies for a longer period at more types of site are also necessary. Securing a more
477 reliable *a priori* database is expected to improve the OE-based aerosol retrieval algorithm.

478

479 **Acknowledgements**

480 This research was supported by the GEMS program of the Ministry of Environment, Korea and the
481 Eco Innovation Program of KEITI (2012000160002). The authors also acknowledge the KNMI and
482 NASA/GSFC for providing OMI and AERONET data.

483

484 **References**

- 485 Ahn, C., Torres, O., and Bhartia, P. K.: Comparison of ozone monitoring instrument UV aerosol
486 products with Aqua/Moderate Resolution Imaging Spectroradiometer and Multiangle Imaging
487 Spectroradiometer observations in 2006, *J Geophys Res-Atmos*, 113, Artn D16s27 Doi
488 10.1029/2007jd008832, 2008.
- 489 Ahn, C., Torres, O., and Jethva, H.: Assessment of OMI near-UV aerosol optical depth over land, *J*
490 *Geophys Res-Atmos*, 119, 2457-2473, Doi 10.1002/2013jd020188, 2014.
- 491 Al-Saadi, J., Szykman, J., Pierce, R. B., Kittaka, C., Neil, D., Chu, D. A., Remer, L., Gumley, L.,
492 Prins, E., Weinstock, L., MacDonald, C., Wayland, R., Dimmick, F., and Fishman, J.:
493 Improving national air quality forecasts with satellite aerosol observations, *B Am Meteorol*
494 *Soc*, 86, 1249-+, Doi 10.1175/Bams-86-9-1249, 2005.
- 495 Breon, F. M., Tanre, D., and Generoso, S.: Aerosol effect on cloud droplet size monitored from
496 satellite, *Science*, 295, 834-838, DOI 10.1126/science.1066434, 2002.
- 497 Chahine, M. T.: Determination of temperature profile in an atmosphere from its outgoing radiance,
498 *J. Opt. Soc. Am.*, 12, 1634-1637, 1968.
- 499 Curier, R. L., Veefkind, J. P., Braak, R., Veihelmann, B., Torres, O., and de Leeuw, G.: Retrieval of
500 aerosol optical properties from OMI radiances using a multiwavelength algorithm: Application
501 to western Europe, *J Geophys Res-Atmos*, 113, Artn D17s90 Doi 10.1029/2007jd008738,
502 2008.
- 503 de Graaf, M., Stammes, P., Torres, O., and Koelemeijer, R. B. A.: Absorbing Aerosol Index:
504 Sensitivity analysis, application to GOME and comparison with TOMS, *J Geophys Res-Atmos*,
505 110, Artn D01201 Doi 10.1029/2004jd005178, 2005.
- 506 Deuze, J. L., Breon, F. M., Devaux, C., Goloub, P., Herman, M., Lafrance, B., Maignan, F.,
507 Marchand, A., Nadal, F., Perry, G., and Tanre, D.: Remote sensing of aerosols over land
508 surfaces from POLDER-ADEOS-1 polarized measurements, *J Geophys Res-Atmos*, 106,

509 4913-4926, Doi 10.1029/2000jd900364, 2001.

510 Dobber, M. R., Dirksen, R. J., Levelt, P. F., Van den Oord, G. H. J., Voors, R. H. M., Kleipool, Q.,
511 Jaross, G., Kowalewski, M., Hilsenrath, E., Leppelmeier, G. W., de Vries, J., Dierssen, W.,
512 and Rozemeijer, N. C.: Ozone-Monitoring Instrument calibration, *Ieee T Geosci Remote*, 44,
513 1209-1238, Doi 10.1109/Tgrs.2006.869987, 2006.

514 Dubovik, O., and King, M. D.: A flexible inversion algorithm for retrieval of aerosol optical
515 properties from Sun and sky radiance measurements, *J Geophys Res-Atmos*, 105, 20673-
516 20696, Doi 10.1029/2000jd900282, 2000.

517 Dubovik, O., Smirnov, A., Holben, B. N., King, M. D., Kaufman, Y. J., Eck, T. F., and Slutsker, I.:
518 Accuracy assessments of aerosol optical properties retrieved from Aerosol Robotic Network
519 (AERONET) Sun and sky radiance measurements, *J Geophys Res-Atmos*, 105, 9791-9806,
520 Doi 10.1029/2000jd900040, 2000.

521 Dubovik, O.: Optimization of numerical inversion in photopolarimetric remote sensing,
522 *Photopolarimetry in Remote Sensing*, 65-106, 2004.

523 Dubovik, O., Sinyuk, A., Lapyonok, T., Holben, B. N., Mishchenko, M., Yang, P., Eck, T. F.,
524 Volten, H., Munoz, O., Veihelmann, B., van der Zande, W. J., Leon, J. F., Sorokin, M., and
525 Slutsker, I.: Application of spheroid models to account for aerosol particle nonsphericity in
526 remote sensing of desert dust, *J Geophys Res-Atmos*, 111, Artn D11208 Doi
527 10.1029/2005jd006619, 2006.

528 Eyre, J. R.: On Systematic-Errors in Satellite Sounding Products and Their Climatological Mean-
529 Values, *Q J Roy Meteor Soc*, 113, 279-292, Doi 10.1256/Smsqj.47515, 1987.

530 Fisher: On the "probable error" of a coefficient of correlation deduced from a small sample, *Metron*,
531 1, 3-32, 1921.

532 Fisher, D., Muller, J. P., and Yershov, V. N.: Automated Stereo Retrieval of Smoke Plume Injection
533 Heights and Retrieval of Smoke Plume Masks From AATSR and Their Assessment With

534 CALIPSO and MISR, *Ieee T Geosci Remote*, 52, 1249-1258, Doi 10.1109/Tgrs.2013.2249073,
535 2014.

536 Govaerts, Y. M., Wagner, S., Lattanzio, A., and Watts, P.: Joint retrieval of surface reflectance and
537 aerosol optical depth from MSG/SEVIRI observations with an optimal estimation approach: 1.
538 Theory, *J Geophys Res-Atmos*, 115, Artn D02203 Doi 10.1029/2009jd011779, 2010.

539 Herman, J. R., Bhartia, P. K., Torres, O., Hsu, C., Seftor, C., and Celarier, E.: Global distribution of
540 UV-absorbing aerosols from Nimbus 7/TOMS data, *J Geophys Res-Atmos*, 102, 16911-16922,
541 Doi 10.1029/96jd03680, 1997.

542 Hess, M., Koepke, P., and Schult, I.: Optical properties of aerosols and clouds: The software
543 package OPAC, *B Am Meteorol Soc*, 79, 831-844, Doi 10.1175/1520-
544 0477(1998)079<0831:Opoaac>2.0.Co;2, 1998.

545 Holben, B. N., Eck, T. F., Slutsker, I., Tanre, D., Buis, J. P., Setzer, A., Vermote, E., Reagan, J. A.,
546 Kaufman, Y. J., Nakajima, T., Lavenu, F., Jankowiak, I., and Smirnov, A.: AERONET - A
547 federated instrument network and data archive for aerosol characterization, *Remote Sens*
548 *Environ*, 66, 1-16, Doi 10.1016/S0034-4257(98)00031-5, 1998.

549 Jaross, G.: discussion of OMI BSDF calibration accuracy, in, edited by: Jeong, U., SSAI, Lanham,
550 Maryland, USA, 2015.

551 Jeong, U., Kim, J., Lee, H., Jung, J., Kim, Y. J., Song, C. H., and Koo, J. H.: Estimation of the
552 contributions of long range transported aerosol in East Asia to carbonaceous aerosol and PM
553 concentrations in Seoul, Korea using highly time resolved measurements: a PSCF model
554 approach, *J Environ Monitor*, 13, 1905-1918, Doi 10.1039/C0em00659a, 2011.

555 Jethva, H., and Torres, O.: Satellite-based evidence of wavelength-dependent aerosol absorption in
556 biomass burning smoke inferred from Ozone Monitoring Instrument, *Atmos Chem Phys*, 11,
557 10541-10551, DOI 10.5194/acp-11-10541-2011, 2011.

558 Jethva, H., Torres, O., and Ahn, C.: Global assessment of OMI aerosol single-scattering albedo

559 using ground-based AERONET inversion, *J Geophys Res-Atmos*, 119, 9020-9040, Doi
560 10.1002/2014jd021672, 2014.

561 Kalman, R. E.: A new approach to linear filtering and prediction problems, *Journal of Basic*
562 *Engineering*, 82, 35-45, 1960.

563 Kim, J., Lee, J., Lee, H. C., Higurashi, A., Takemura, T., and Song, C. H.: Consistency of the
564 aerosol type classification from satellite remote sensing during the Atmospheric Brown Cloud-
565 East Asia Regional Experiment campaign, *J Geophys Res-Atmos*, 112, Artn D22s33 Doi
566 10.1029/2006jd008201, 2007.

567 Kinne, S., Schulz, M., Textor, C., Guibert, S., Balkanski, Y., Bauer, S. E., Bernsten, T., Berglen, T.
568 F., Boucher, O., Chin, M., Collins, W., Dentener, F., Diehl, T., Easter, R., Feichter, J.,
569 Fillmore, D., Ghan, S., Ginoux, P., Gong, S., Grini, A., Hendricks, J. E., Herzog, M., Horowitz,
570 L., Isaksen, I., Iversen, T., Kirkavag, A., Kloster, S., Koch, D., Kristjansson, J. E., Krol, M.,
571 Lauer, A., Lamarque, J. F., Lesins, G., Liu, X., Lohmann, U., Montanaro, V., Myhre, G.,
572 Penner, J. E., Pitari, G., Reddy, S., Seland, O., Stier, P., Takemura, T., and Tie, X.: An
573 AeroCom initial assessment - optical properties in aerosol component modules of global
574 models, *Atmos Chem Phys*, 6, 1815-1834, 2006.

575 Kirchstetter, T. W., Novakov, T., and Hobbs, P. V.: Evidence that the spectral dependence of light
576 absorption by aerosols is affected by organic carbon, *J Geophys Res-Atmos*, 109, Artn D21208
577 Doi 10.1029/2004jd004999, 2004.

578 Lee, J., Kim, J., Yang, P., and Hsu, N. C.: Improvement of aerosol optical depth retrieval from
579 MODIS spectral reflectance over the global ocean using new aerosol models archived from
580 AERONET inversion data and tri-axial ellipsoidal dust database, *Atmos Chem Phys*, 12, 7087-
581 7102, DOI 10.5194/acp-12-7087-2012, 2012.

582 Levelt, P. F., Van den Oord, G. H. J., Dobber, M. R., Malkki, A., Visser, H., de Vries, J., Stammes,
583 P., Lundell, J. O. V., and Saari, H.: The Ozone Monitoring Instrument, *Ieee T Geosci Remote*,

584 44, 1093-1101, Doi 10.1109/Tgrs.2006.872333, 2006.

585 Levy, R. C., Remer, L. A., Mattoo, S., Vermote, E. F., and Kaufman, Y. J.: Second-generation
586 operational algorithm: Retrieval of aerosol properties over land from inversion of Moderate
587 Resolution Imaging Spectroradiometer spectral reflectance, *J Geophys Res-Atmos*, 112, Artn
588 D13211 Doi 10.1029/2006jd007811, 2007.

589 Lin, J. T., Martin, R. V., Boersma, K. F., Sneep, M., Stammes, P., Spurr, R., Wang, P., Van
590 Roozendaal, M., Clemer, K., and Irie, H.: Retrieving tropospheric nitrogen dioxide from the
591 Ozone Monitoring Instrument: effects of aerosols, surface reflectance anisotropy, and vertical
592 profile of nitrogen dioxide, *Atmos Chem Phys*, 14, 1441-1461, DOI 10.5194/acp-14-1441-
593 2014, 2014.

594 Livingston, J. M., Redemann, J., Russell, P. B., Torres, O., Veihelmann, B., Veefkind, P., Braak, R.,
595 Smirnov, A., Remer, L., Bergstrom, R. W., Coddington, O., Schmidt, K. S., Pilewskie, P.,
596 Johnson, R., and Zhang, Q.: Comparison of aerosol optical depths from the Ozone Monitoring
597 Instrument (OMI) on Aura with results from airborne sunphotometry, other space and ground
598 measurements during MILAGRO/INTEX-B, *Atmos Chem Phys*, 9, 6743-6765, 2009.

599 Mishchenko, M. I., and Travis, L. D.: T-Matrix Computations of Light-Scattering by Large
600 Spheroidal Particles, *Opt Commun*, 109, 16-21, Doi 10.1016/0030-4018(94)90731-5, 1994.

601 Mishchenko, M. I., Lacis, A. A., Carlson, B. E., and Travis, L. D.: Nonsphericity of Dust-Like
602 Tropospheric Aerosols - Implications for Aerosol Remote-Sensing and Climate Modeling,
603 *Geophys Res Lett*, 22, 1077-1080, Doi 10.1029/95gl00798, 1995.

604 Mishchenko, M. I., Travis, L. D., Kahn, R. A., and West, R. A.: Modeling phase functions for
605 dustlike tropospheric aerosols using a shape mixture of randomly oriented polydisperse
606 spheroids, *J Geophys Res-Atmos*, 102, 16831-16847, Doi 10.1029/96jd02110, 1997.

607 Mishchenko, M. I., Geogdzhayev, I. V., Liu, L., Ogren, J. A., Lacis, A. A., Rossow, W. B.,
608 Hovenier, J. W., Volten, H., and Munoz, O.: Aerosol retrievals from AVHRR radiances:

609 effects of particle nonsphericity and absorption and an updated long-term global climatology
610 of aerosol properties, *J Quant Spectrosc Ra*, 79, 953-972, Doi 10.1016/S0022-4073(02)00331-
611 X, 2003.

612 Palmer, P. I., Jacob, D. J., Chance, K., Martin, R. V., Spurr, R. J. D., Kurosu, T. P., Bey, I.,
613 Yantosca, R., Fiore, A., and Li, Q. B.: Air mass factor formulation for spectroscopic
614 measurements from satellites: Application to formaldehyde retrievals from the Global Ozone
615 Monitoring Experiment, *J Geophys Res-Atmos*, 106, 14539-14550, Doi
616 10.1029/2000jd900772, 2001.

617 Phillips, B. L.: A technique for numerical solution of certain intergral equation of first kind, *Journal*
618 *of Assoc. Comput. Mach.*, 9, 84-97, 1962.

619 Ramanathan, V., Crutzen, P. J., Kiehl, J. T., and Rosenfeld, D.: Atmosphere - Aerosols, climate,
620 and the hydrological cycle, *Science*, 294, 2119-2124, DOI 10.1126/science.1064034, 2001.

621 Rodgers, C. D.: Characterization and Error Analysis of Profiles Retrieved from Remote Sounding
622 Measurements, *J Geophys Res-Atmos*, 95, 5587-5595, Doi 10.1029/Jd095id05p05587, 1990.

623 Rodgers, C. D.: Inverse method for atmospheric sounding: theory and practice, World Scientific
624 Publishing Co. Pte. Ltd., Singapore, 2000.

625 Russell, P. B., Hobbs, P. V., and Stowe, L. L.: Aerosol properties and radiative effects in the United
626 States East Coast haze plume: An overview of the Tropospheric Aerosol Radiative Forcing
627 Observational Experiment (TARFOX), *J Geophys Res-Atmos*, 104, 2213-2222, Doi
628 10.1029/1998jd200028, 1999.

629 Russell, P. B., Bergstrom, R. W., Shinozuka, Y., Clarke, A. D., DeCarlo, P. F., Jimenez, J. L.,
630 Livingston, J. M., Redemann, J., Dubovik, O., and Strawa, A.: Absorption Angstrom Exponent
631 in AERONET and related data as an indicator of aerosol composition, *Atmos Chem Phys*, 10,
632 1155-1169, 2010.

633 Spurr, R., Wang, J., Zeng, J., and Mishchenko, M. I.: Linearized T-matrix and Mie scattering

634 computations, *J Quant Spectrosc Ra*, 113, 425-439, 10.1016/j.jqsrt.2011.11.014, 2012.

635 Spurr, R., and Christi, M.: On the generation of atmospheric property Jacobians from the
636 (V)LIDORT linearized radiative transfer models, *J Quant Spectrosc Ra*, 142, 109-115,
637 10.1016/j.jqsrt.2014.03.011, 2014.

638 Spurr, R. J. D.: VLIDORT: A linearized pseudo-spherical vector discrete ordinate radiative transfer
639 code for forward model and retrieval studies in multilayer multiple scattering media, *J Quant
640 Spectrosc Ra*, 102, 316-342, DOI 10.1016/j.jqsrt.2006.05.005, 2006.

641 Tikhonov, A. N.: On the solution of incorrectly stated problems and a method of regularization,
642 *Dokl. Akad. Nauk.*, 151, 501-504, 1963.

643 Torres, O., Bhartia, P. K., Herman, J. R., Ahmad, Z., and Gleason, J.: Derivation of aerosol
644 properties from satellite measurements of backscattered ultraviolet radiation: Theoretical basis
645 (vol 103, pg 17099, 1998), *J Geophys Res-Atmos*, 103, 23321-23321, 1998.

646 Torres, O., Bhartia, P. K., Herman, J. R., Sinyuk, A., Ginoux, P., and Holben, B.: A long-term
647 record of aerosol optical depth from TOMS observations and comparison to AERONET
648 measurements, *J Atmos Sci*, 59, 398-413, Doi 10.1175/1520-
649 0469(2002)059<0398:Altro>2.0.Co;2, 2002a.

650 Torres, O., Decae, R., Veefkind, J. P., and de Leeuw, G.: OMI aerosol retrieval algorithm, in *OMI
651 Algorithm Theoretical Basis Document*, NASA Goddard Space Flight Cent., Greenbelt, Md.,
652 USA, 47-71, 2002b.

653 Torres, O., Bhartia, P. K., Sinyuk, A., Welton, E. J., and Holben, B.: Total Ozone Mapping
654 Spectrometer measurements of aerosol absorption from space: Comparison to SAFARI 2000
655 ground-based observations, *J Geophys Res-Atmos*, 110, Artn D10s18 Doi 10.1029/Jd004611,
656 2005.

657 Torres, O., Tanskanen, A., Veihelmann, B., Ahn, C., Braak, R., Bhartia, P. K., Veefkind, P., and
658 Levelt, P.: Aerosols and surface UV products from Ozone Monitoring Instrument observations:

659 An overview, *J Geophys Res-Atmos*, 112, Artn D24s47 Doi 10.1029/2007jd008809, 2007.

660 Torres, O., Ahn, C., and Chen, Z.: Improvements to the OMI near-UV aerosol algorithm using A-
661 train CALIOP and AIRS observations, *Atmos Meas Tech*, 6, 3257-3270, DOI 10.5194/amt-6-
662 3257-2013, 2013.

663 Twomey, S.: On the numerical solution of Fredholm integral equations of the first kind by the
664 inversion of the linear system produced by quadrature, *Journal of Assoc. Comput. Mach.*, 10,
665 97-101, 1963.

666 Veihelmann, B., Levelt, P. F., Stammes, P., and Veeffkind, J. P.: Simulation study of the aerosol
667 information content in OMI spectral reflectance measurements, *Atmos Chem Phys*, 7, 3115-
668 3127, 2007.

669 Wagner, S. C., Govaerts, Y. M., and Lattanzio, A.: Joint retrieval of surface reflectance and aerosol
670 optical depth from MSG/SEVIRI observations with an optimal estimation approach: 2.
671 Implementation and evaluation, *J Geophys Res-Atmos*, 115, Artn D02204 Doi
672 10.1029/2009jd011780, 2010.

673 Wurl, D., Grainger, R. G., McDonald, A. J., and Deshler, T.: Optimal estimation retrieval of aerosol
674 microphysical properties from SAGE II satellite observations in the volcanically unperturbed
675 lower stratosphere, *Atmos Chem Phys*, 10, 4295-4317, DOI 10.5194/acp-10-4295-2010, 2010.

676 Young, S. A., Vaughan, M. A., Kuehn, R. E., and Winker, D. M.: The Retrieval of Profiles of
677 Particulate Extinction from Cloud-Aerosol Lidar and Infrared Pathfinder Satellite Observations
678 (CALIPSO) Data: Uncertainty and Error Sensitivity Analyses, *J Atmos Ocean Tech*, 30, 395-
679 428, Doi 10.1175/Jtech-D-12-00046.1, 2013.

680

681 **Tables and Figures**

682 **Table captions**

683 **Table 1.** Positions and mean AOT and SSA at 388 nm of the AERONET sites during the
684 DRAGON-NE Asia 2012 campaign.

685 **Table 2.** Aerosol number-size distribution parameters* and real refractive index (n_r) for each
686 aerosol type in the OMI near-UV algorithm.

687 **Table 3.** Retrieval approach criteria of OMI near-UV algorithm version 1.5.3.

688 **Table 4.** Diagonal and off-diagonal elements of the measurement error covariance matrices using
689 two different measurement matrices.

690 **Table 5.** Error sources and their assumed magnitudes in the OMI ATBD (Algorithm Theoretical
691 Basis Documents) and this study.

692

693

694 **List of tables**

695 **Table 1.** Positions and mean AOT and SSA at 388 nm of the AERONET sites during the
 696 DRAGON-NE Asia 2012 campaign.

Site name	Latitude (°) (North)	Longitude (°) (East)	Mean 380 nm AOT	Mean 440 nm SSA
Baengnyeong	37.97	124.63	0.56	0.96
Yonsei Univ., Seoul	37.56	126.94	0.63	0.93
Anmyeon	36.54	126.33	0.57	0.94
Bokjeong, Seoul	37.46	127.13	0.75	0.90
Gangneung Wonju National Univ.	37.77	128.87	0.53	0.92
Guwol, Seoul	37.45	126.72	0.69	0.94
GIST, Gwangju	35.23	126.84	0.54	0.93
HUFS, Yongin	37.34	127.27	0.63	0.90
Kongju National Univ., Kongju	36.47	127.14	0.62	0.96
Konkuk Univ., Seoul	37.54	127.08	0.67	0.92
Korea Univ., Seoul	37.59	127.03	0.73	0.92
Kunsan National Univ., Kunsan	35.94	126.68	0.61	0.92
Kyungil Univ., Kyungsan	36.07	128.82	0.57	0.93
Mokpo National Univ., Mokpo	34.91	126.44	0.58	0.93
NIER, Incheon	37.57	126.64	0.62	0.93
Pusan National Univ., Pusan	35.24	129.08	0.62	0.93
Sanggye, Seoul	37.66	127.07	0.73	0.92
Sinjeong, Seoul	37.52	126.86	0.64	0.91
Soha, Seoul	37.45	126.89	0.69	0.91
Gosan, Jeju	33.29	126.16	0.62	0.96
Seoul National Univ., Seoul	37.46	126.95	0.65	0.93
Fukuoka	33.52	130.48	0.50	0.90
Kohriyama	37.36	140.38	0.34	0.95
Kyoto	35.03	135.78	0.47	0.94
Matsue	35.48	133.01	0.56	0.93
Mt. Ikoma	34.68	135.68	0.39	0.96
Mt. Rokko	34.76	135.23	0.41	0.95
Nara	34.69	135.83	0.48	0.94
Nishiharima	35.03	134.34	0.42	0.95
North Osaka	34.77	135.51	0.52	0.94
South Osaka	34.54	135.50	0.55	0.94

Tsukuba	36.05	140.12	0.38	0.94
Noto	37.33	137.14	0.41	0.94
Shirahama	33.69	135.36	0.41	0.96
Chiba University	35.63	140.10	0.31	0.92
Fukue	32.75	128.68	0.78	0.92

697

698

699

700

701 **Table 2.** Aerosol number-size distribution parameters* and real refractive index (n_r) for each
 702 aerosol type in the OMI near-UV algorithm.

Aerosol Model	r_g m1 [μm]	r_g m2 [μm]	σ m1 [μm]	σ m2 [μm]	FMF	n_r	$n_{i,354/388}$
Sulfate	0.088	0.509	1.499	2.160	0.999596	1.40	1.0
Smoke	0.080	0.705	1.492	2.075	0.999795	1.50	1.2
Dust	0.052	0.670	1.697	1.806	0.995650	1.55	1.4

703 *Number-weighted particle size distribution parameters: fine and coarse mode radii (r_g m1 and r_g
 704 m2) and variance (σ m1 and σ m2), number fine mode fraction (FMF).
 705

706

707

708 **Table 3.** Retrieval approach criteria of OMI near-UV algorithm version 1.5.3.

Surface Category	UVAI	CO (10^{18} molecules- cm^{-2})	Surface Type	Aerosol Type	Retrieval Approach
Ocean	≥ 0.5	> 2.2 NH (1.8 SH)	N/A*	Smoke	Two-channel
Ocean	≥ 0.5	≤ 2.2 NH (1.8 SH)	N/A	Dust	Two-channel
Ocean	< 0.5	-	-	-	No retrieval
Land	≥ 0.5	> 2.2 NH (1.8 SH)	All	Smoke	Two-channel
Land	≥ 0.5	≤ 2.2 NH (1.8 SH)	All	Dust	Two-channel
Land	< 0.5	> 2.2 NH (1.8 SH)	All	Sulfate	Two-channel
Land	< 0.5	≤ 2.2 NH (1.8 SH)	All but arid	Sulfate	Single channel
Land	< 0.5	≤ 2.2 NH (1.8 SH)	arid	Dust	Single Channel

709 *Not available.
 710

711 **Table 4.** Diagonal and off-diagonal elements of the measurement error covariance matrices using
 712 two different measurement matrices.

Measurement matrix	$[I_{354} \ I_{388}]^T$	$\begin{bmatrix} I_{354} & I_{354} \\ I_{388} & I_{388} \end{bmatrix}^T$
First diagonal term	$\sigma(\epsilon_{354})^2$	$\sigma(\epsilon_{388})^2$
Second diagonal term	$\sigma(\epsilon_{388})^2$	$\left(\frac{I_{354}}{I_{388}}\right)^2 \left\{ \left(\frac{\epsilon_{r,354}}{I_{354}}\right)^2 + \left(\frac{\epsilon_{r,388}}{I_{388}}\right)^2 \right\}$
Off-diagonal term	$\sigma(\epsilon_{354}, \epsilon_{388})^2$	0

713

714 **Table 5.** Error sources and their assumed magnitudes in the OMI ATBD (Algorithm Theoretical
715 Basis Documents) and this study.

Error source	Error perturbation (OMI ATBD)	Assumed value of σ for each error source in this study
Cloud Contamination	5% cloud contamination	NA ⁺
Surface Reflectivity	0.01 error in surface reflectivity	0.01 for both wavelengths
Radiometric uncertainty	SNR less than 1% Radiometric offset additive error of 1%	1% of BSDF calibration uncertainty (Dobber et al., 2006; Jaross, 2015)
	Radiometric scale factor multiplicative error of 1%	Radiometric precision provided by Level 1b data
Size distribution (mode radius)	5% increase of mode radius	0.019 for fine mode* 0.510 for coarse mode*
Size distribution (width)	5% increase of width	0.265 for fine mode* 0.307 for coarse mode*
Fine mode fraction	NA	0.0015*
Refractive index	Increase with 0.05 for n_r	0.053 for n_r (for all wavelengths and size modes)*
	Increase with 0.01 for n_i	0.0047 for 354 nm n_i *
Aerosol Vertical Profile	Change of 1 km peak height	Change of 2 km peak height Change of 1 km half width
Particle shape	NA	NA

716 *Standard deviation of each parameter during the DRAGON-NE Asia 2012 campaign. The
717 parameters for n_r and n_i were obtained from 440 nm AERONET inversion products.

718 ⁺Not analyzed.

719 **Figure captions**

720 **Figure 1.** Mean 380 nm aerosol optical thickness (AOT) and 440 nm single scattering albedo and
721 their probability density functions during the DRAGON-NE Asia 2012 campaign.

722 **Figure 2.** (a) Mean and (b) standard deviation of 388 nm AOT from the OMAERUV product in
723 spring (March to May) 2005–2014. Panels (c) and (d) show the average and standard deviation of
724 SSA, respectively, during the same period.

725 **Figure 3.** (a) MODIS Aqua true color image and (b) UV aerosol index from the OMI product in
726 Northeast Asia on 28th April 2012.

727 **Figure 4.** (a) OMI operational AOT, (b) OE-based AOT, (c) operational SSA, and (d) OE-based
728 SSA on 28th April 2012 at 388 nm.

729 **Figure 5.** Estimated S_{sn} of (a) OE-based 388 nm AOT and (b) SSA. Panels (c) and (d) show the
730 degrees of freedom and cost function of the retrieval, respectively.

731 **Figure 6.** Validation of 388 nm AOT against AERONET data from (a) operational products and (b)
732 the OE-based algorithm during the DRAGON-NE Asia 2012 campaign.

733 **Figure 7.** Comparison of the 440 nm SSA from AERONET and 388 nm SSA from (a) the
734 operational products and (b) the OE-based algorithm, during the DRAGON-NE Asia 2012
735 campaign. Panels (c) and (d) compare converted 388 nm SSA from AERONET with that from (c)
736 the operational products and (d) the OE-based algorithm.

737 **Figure 8.** Comparison between estimated uncertainties of the 388 nm AOT (x -axis) and biases of
738 retrieved AOT from AERONET measurements (y -axis). The panels (a) and (b) are based on the
739 operational and OE-based retrieval/error-estimation algorithm, respectively.

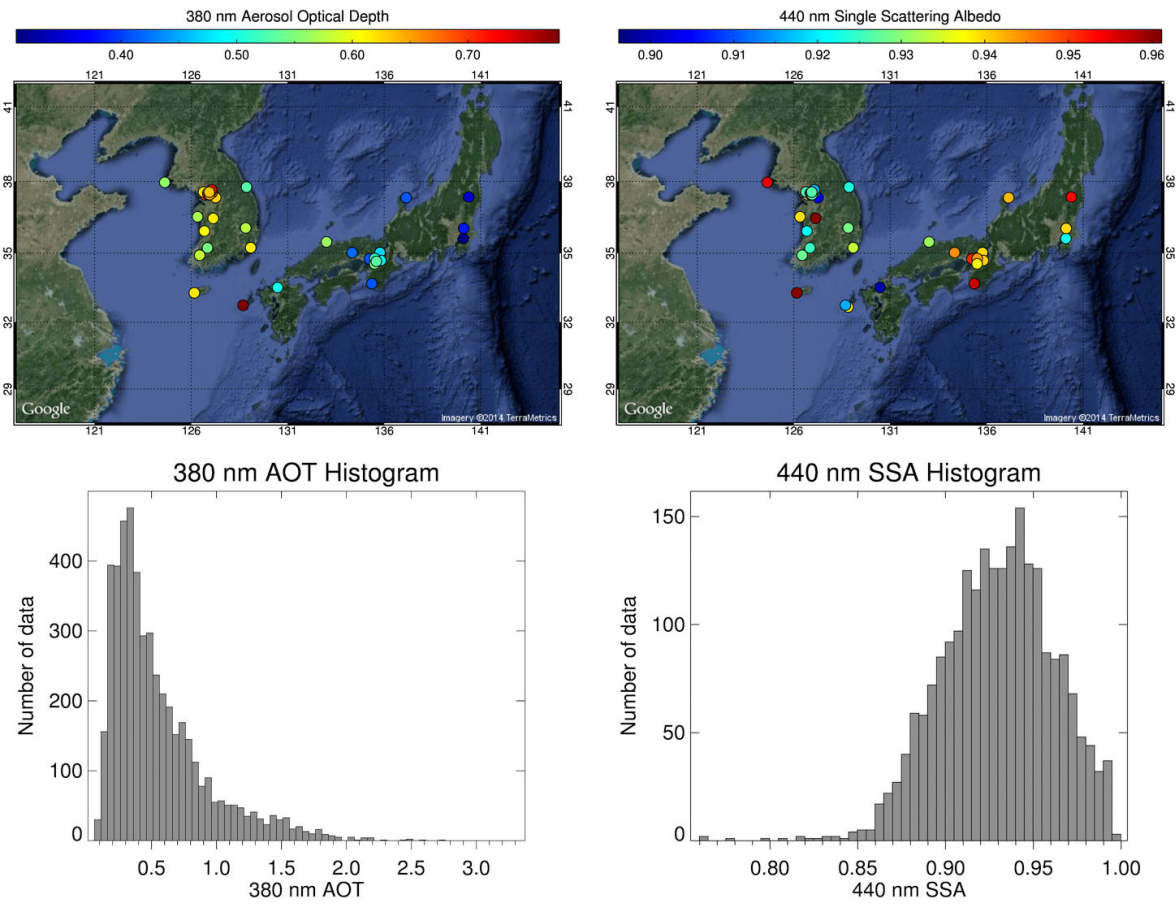
740 **Figure 9.** Average (gray bars) and standard deviation (black lines) of the forward model parameter
741 errors of 388 nm (a) AOT and (b) SSA.

742

743

744 **List of figures**

745 **[Figure 1]**



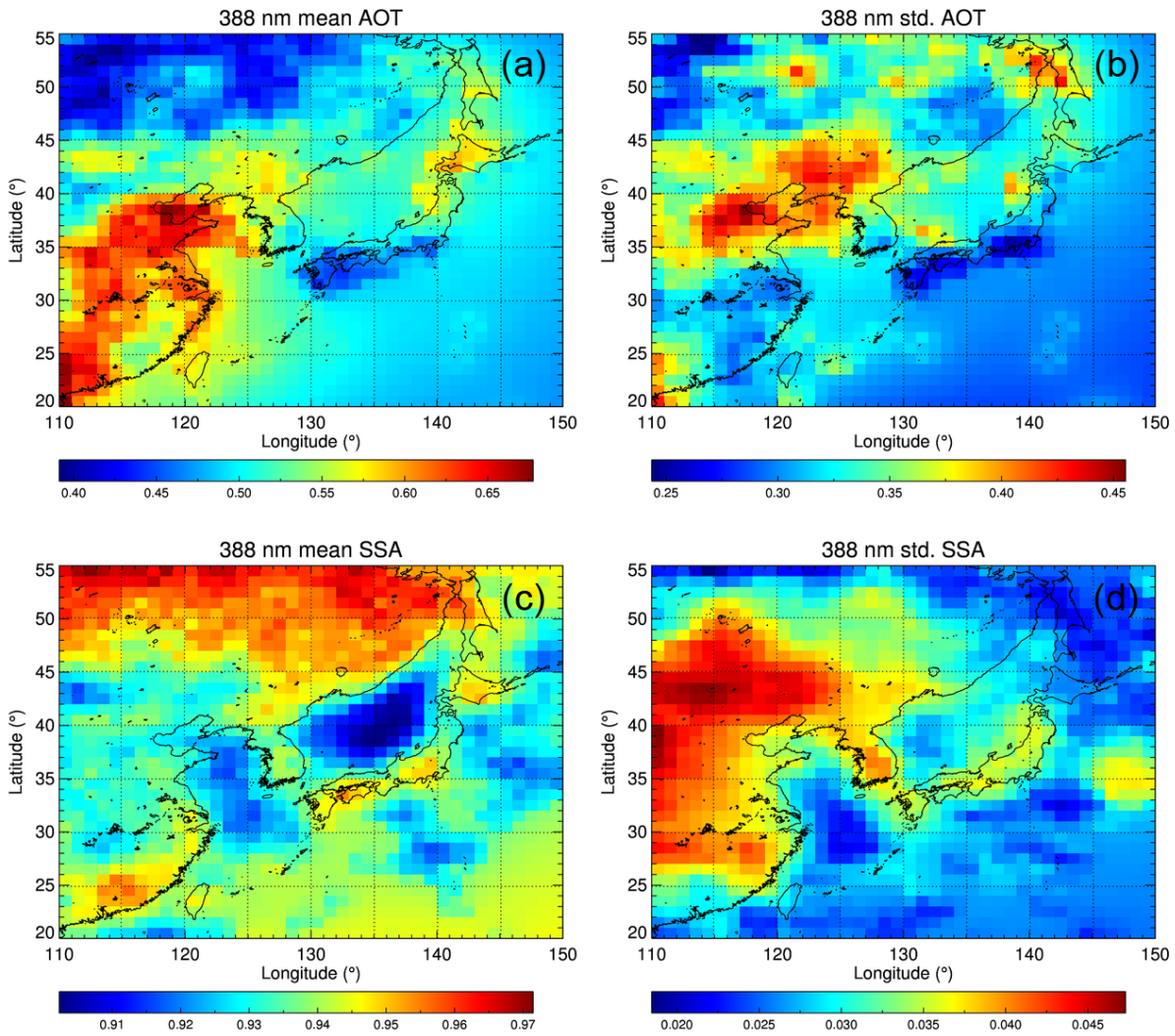
746

747 **Figure 1.** Mean 380 nm aerosol optical thickness (AOT) and 440 nm single scattering albedo and
748 their probability density functions during the DRAGON-NE Asia 2012 campaign.

749

750

751 [Figure 2]

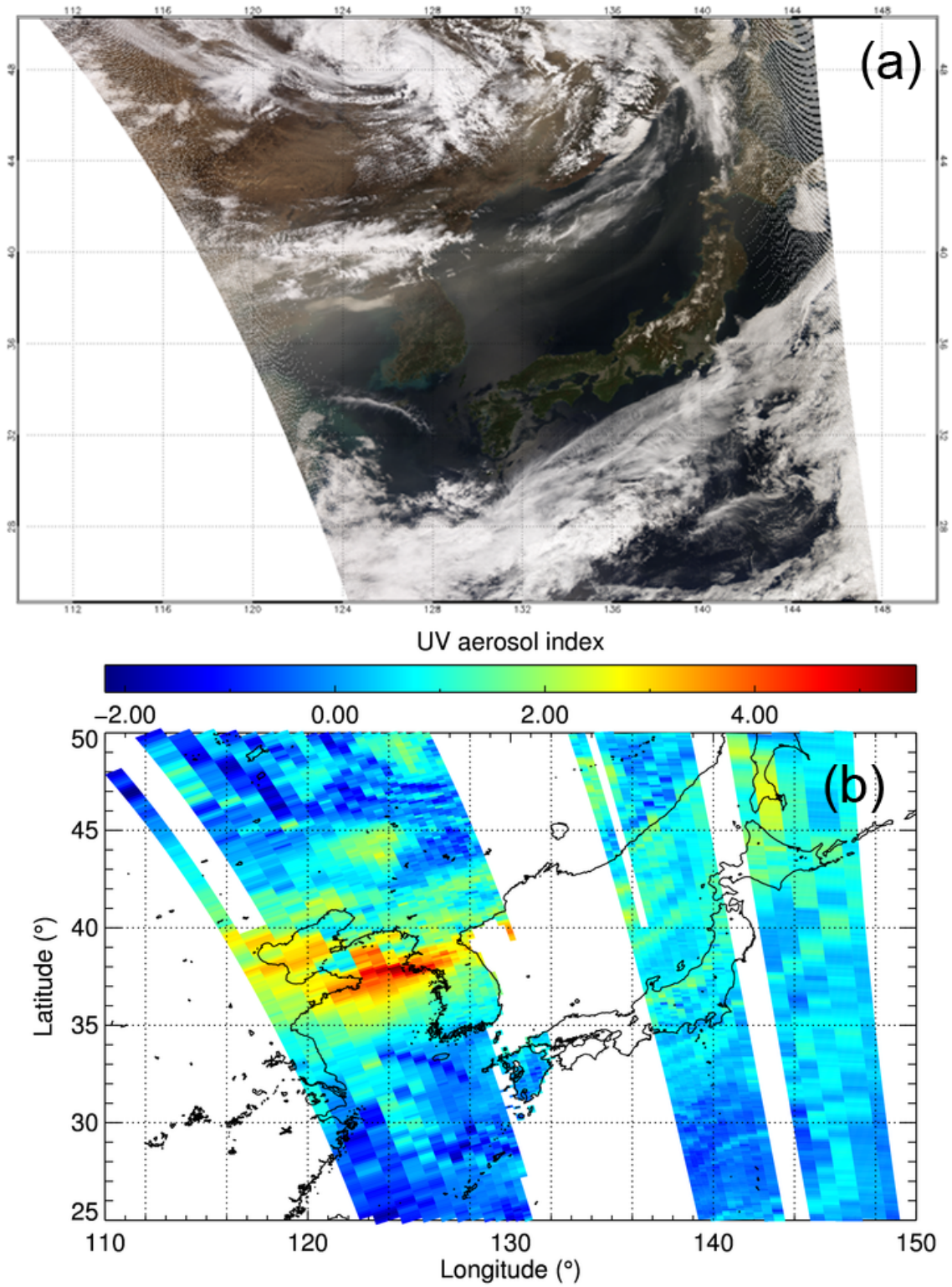


752

753 **Figure 2.** (a) Mean and (b) standard deviation of 388 nm AOT from the OMAERUV product in
754 spring (March to May) 2005–2014. Panels (c) and (d) show the average and standard deviation of
755 SSA, respectively, during the same period.

756

757 [Figure 3]

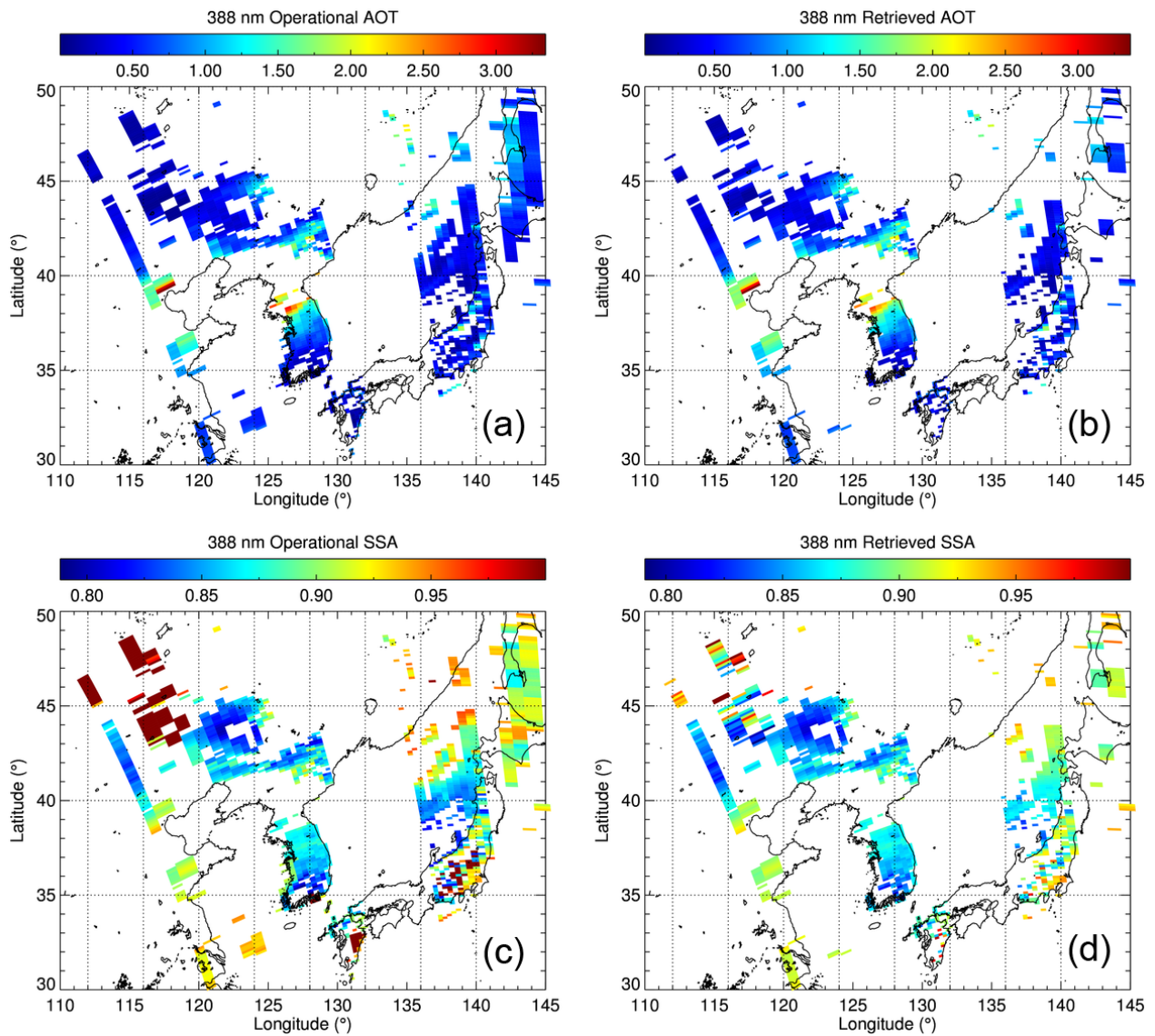


758

759 **Figure 3.** (a) MODIS Aqua true color image and (b) UV aerosol index from the OMI product in

760 Northeast Asia on 28th April 2012.

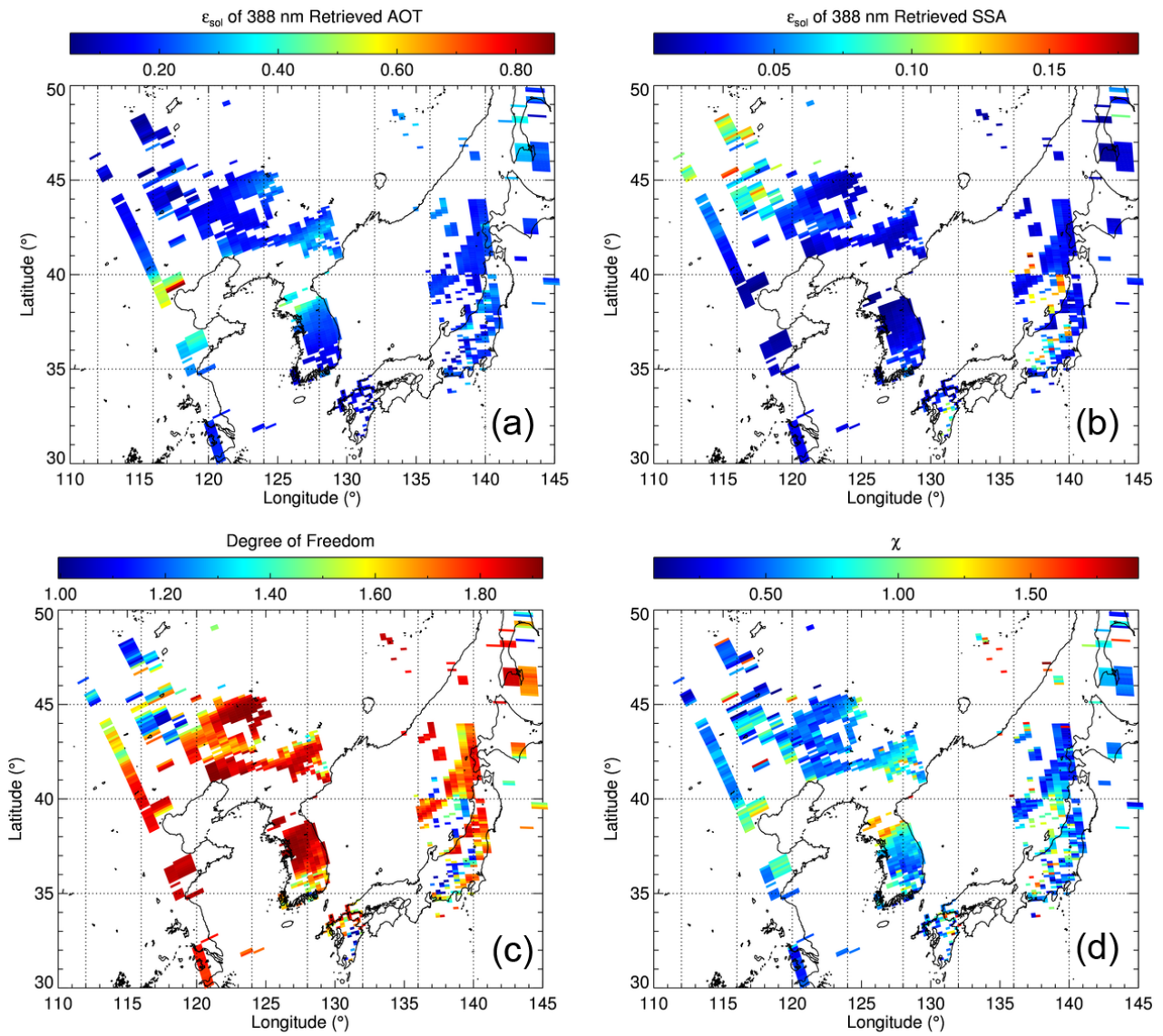
761 [Figure 4]



762

763 **Figure 4.** (a) OMI operational AOT, (b) OE-based AOT, (c) operational SSA, and (d) OE-based
764 SSA on 28th April 2012 at 388 nm.

765 [Figure 5]

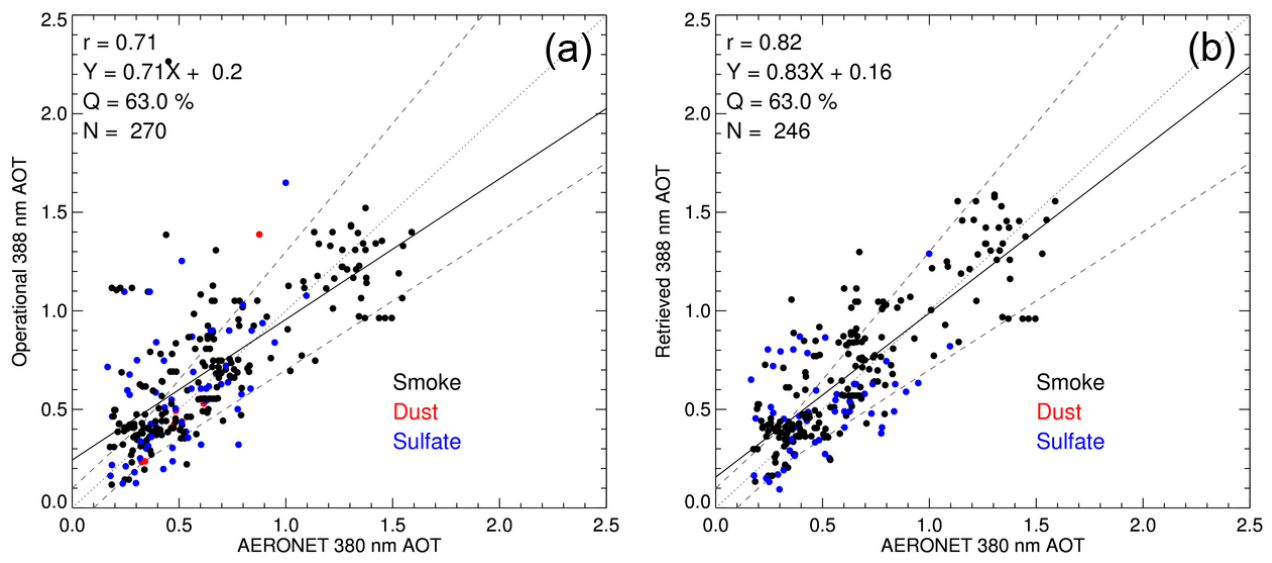


766

767 **Figure 5.** Estimated solution error of (a) OE-based 388 nm AOT and (b) SSA. Panels (c) and (d)
768 show the degrees of freedom and cost function of the retrieval, respectively.

769

770 [Figure 6]



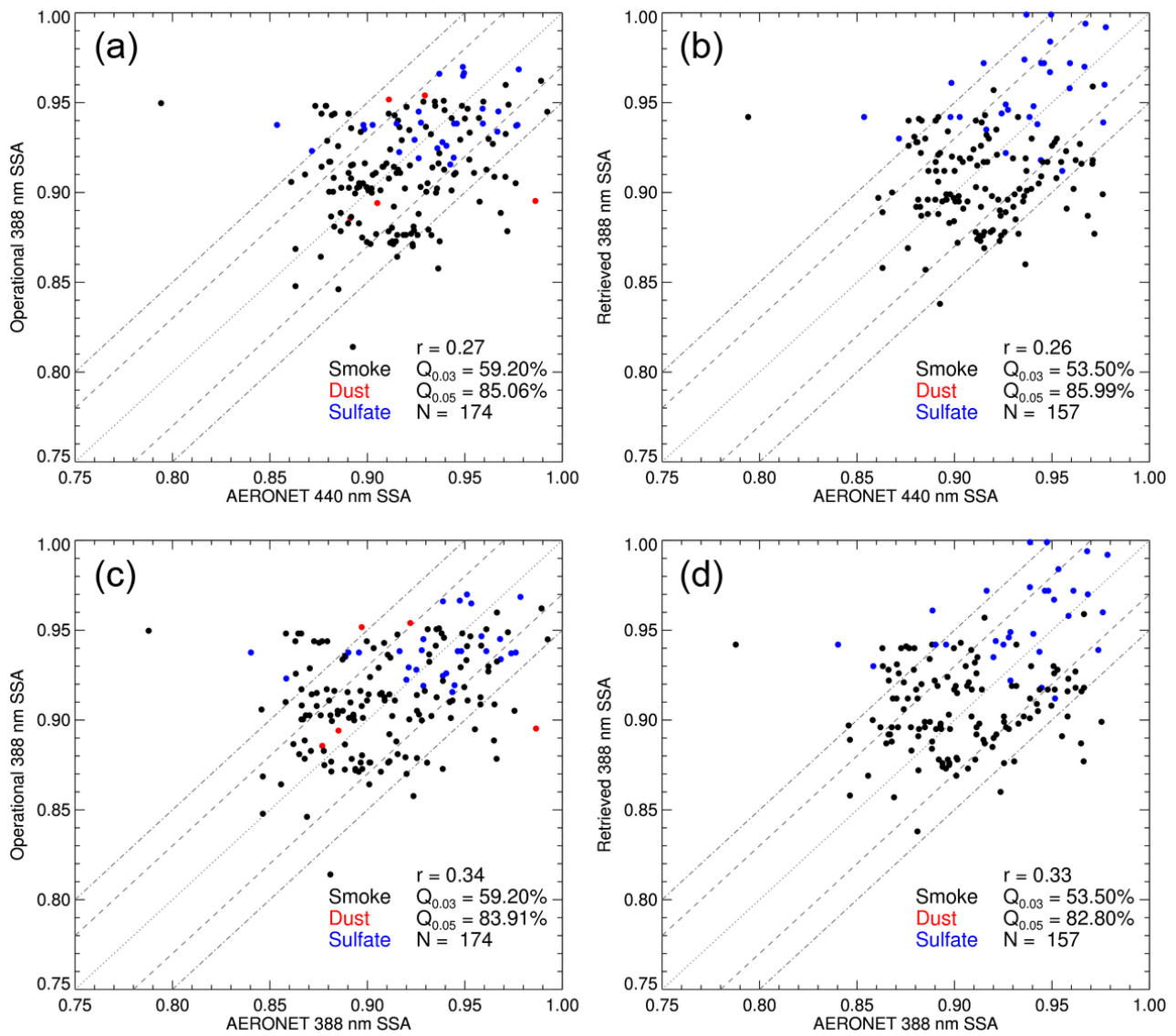
771

772 **Figure 6.** Validation of 388 nm AOT against AERONET data from (a) operational products and (b)

773 the OE-based algorithm during the DRAGON-NE Asia 2012 campaign.

774

775 [Figure 7]

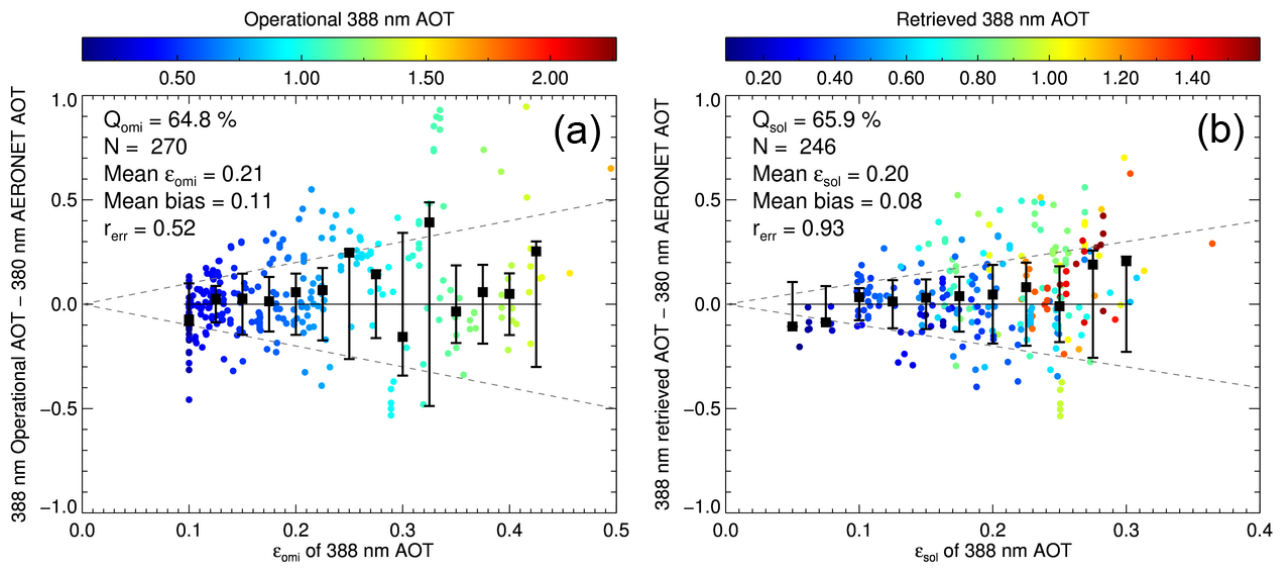


776

777 **Figure 7.** Comparison of the 440 nm SSA from AERONET and 388 nm SSA from (a) the
778 operational products and (b) the OE-based algorithm, during the DRAGON-NE Asia 2012
779 campaign. Panels (c) and (d) compare converted 388 nm SSA from AERONET with that from (c)
780 the operational products and (d) the OE-based algorithm.

781

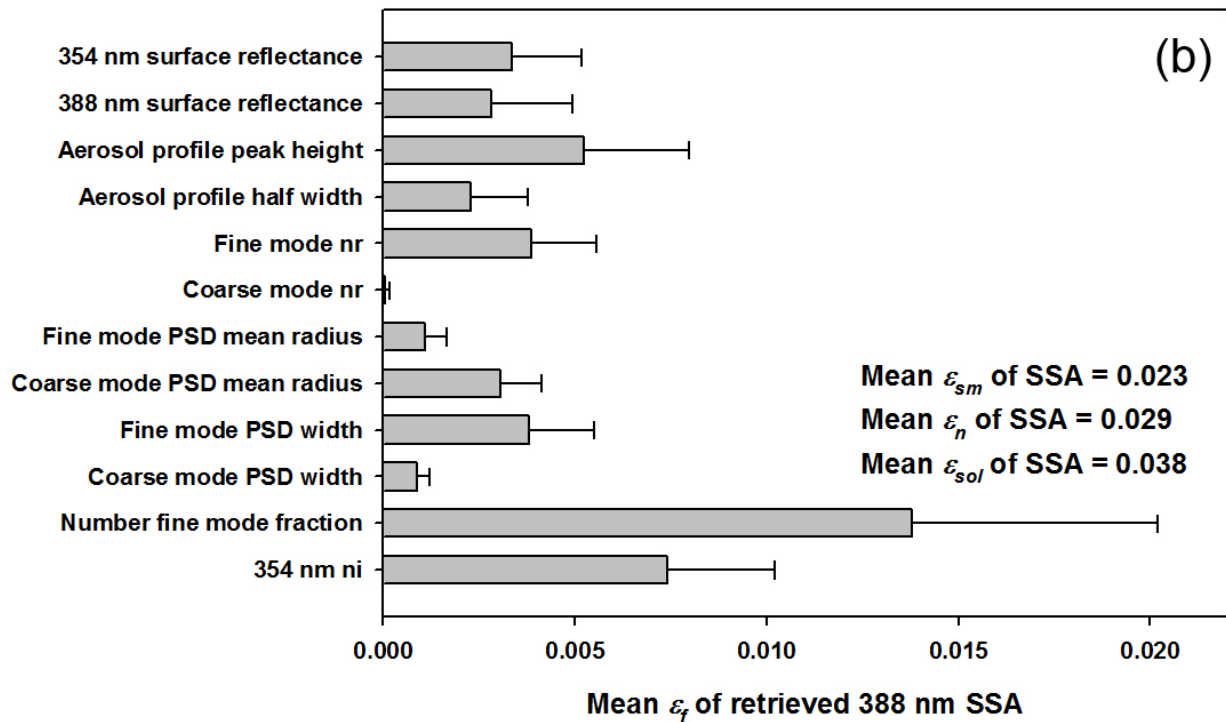
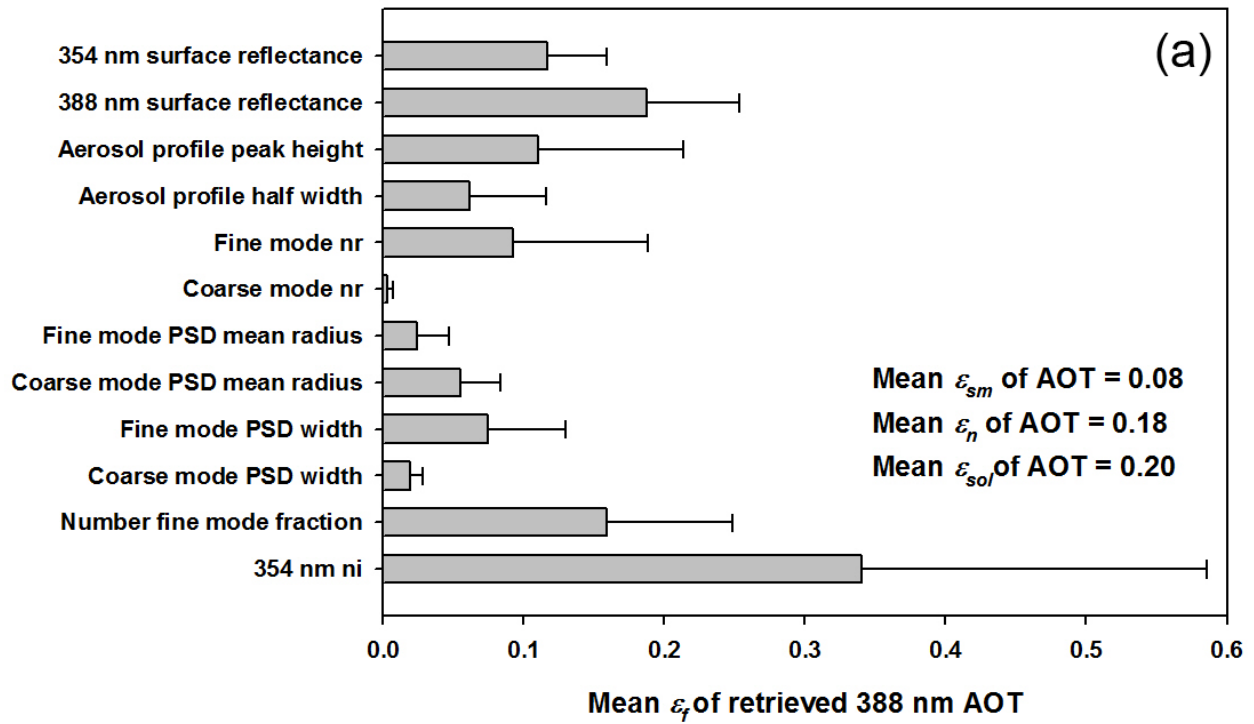
782 [Figure 8]



783

784 **Figure 8.** Comparison between estimated uncertainties of the 388 nm AOT (x -axis) and biases of
785 retrieved AOT from AERONET measurements (y -axis). The panels (a) and (b) are based on the
786 operational and OE-based retrieval/error-estimation algorithm, respectively.

787



789

790 **Figure 9.** Average (gray bars) and standard deviation (black lines) of the forward model parameter

791 errors of 388 nm (a) AOT and (b) SSA.